

Final Technical Report

On

RESEARCH ON SUPERSONIC REACTING FLOWS

AFOSR Grant No. F49620-94-1-0152

Prepared for

AIR FORCE OFFICE OF SCIENTIFIC RESEARCH

For the Period

15 February 1994 to 14 February 1997

Submitted by

**C.T. Bowman
R.K. Hanson
M.G. Mungal
W.C. Reynolds**

DISTRIBUTION STATEMENT A

**Approved for public release;
Distribution Unlimited**

**HIGH TEMPERATURE GASDYNAMICS LABORATORY
Mechanical Engineering Department
Stanford University**

19970604 132

REPORT DOCUMENTATION PAGE

Form Approved
OMB No. 0704-0188

Public reporting burden for this collection of information is estimated to average 1 hour per response, including the time for reviewing instructions, searching existing data sources, gathering and maintaining the data needed, and completing and reviewing the collection of information. Send comments regarding this burden estimate or any other aspect of this collection of information, including suggestions for reducing this burden, to Washington Headquarters Services, Directorate for Information Operations and Reports, 1215 Jefferson Davis Highway, Suite 1204, Arlington, VA 22202-4302, and to the Office of Management and Budget, Paperwork Reduction Project (0704-0188), Washington, DC 20503.

1. AGENCY USE ONLY (Leave Blank)		2. REPORT DATE 14 February 1997		3. REPORT TYPE AND DATES COVERED Final Technical Report 15 February 1994 - 14 February 1997	
4. TITLE AND SUBTITLE Research on Supersonic Reacting Flows				5. FUNDING NUMBERS PE - 61102F PR - 2308 SA - BS G - F49620-94-1-0152	
6. AUTHORS C.T. Bowman, R.K. Hanson M.G. Mungal, W.C. Reynolds				AFOSR-TR-97 0199	
7. PERFORMING ORGANIZATION NAME(S) AND ADDRESS(ES) Stanford University Mechanical Engineering Department Stanford, CA 94305-3032					
8. SPONSORING / MONITORING AGENCY NAME(S) AND ADDRESS(ES) AFOSR/NA 110 Duncan Ave., Suite B115 Bolling AFB, DC 20332-0001				10. SPONSORING / MONITORING AGENCY REPORT NUMBER	
11. SUPPLEMENTARY NOTES					
12a. DISTRIBUTION / AVAILABILITY STATEMENT Approved for public release; distribution is unlimited				12b. DISTRIBUTION CODE	
13. ABSTRACT (Maximum 200 words) An experimental and computational investigation of supersonic combustion flows was carried out. The principal objective of the research was to gain a more fundamental understanding of mixing and chemical reaction in supersonic flows. The research effort comprised three inter-related elements: (1) stability analyses and numerical simulations of compressible reacting flows; (2) development of laser-induced fluorescence techniques for time-resolved multidimensional imaging of species concentration, temperature, velocity and pressure; and (3) an experimental study of mixing and combustion in a supersonic plane mixing layer with the additional development of simple mixing enhancements. The specific objectives and results of the research of each of these program elements have been summarized in this report. New results include: a detailed stability map for reacting, compressible shear layers; new PLIF techniques for transient facilities; new measurements of mixing efficiency in compressible flows and demonstration of simple mixing enhancement techniques with low pressure drop.					
14. SUBJECT TERMS Supersonic Combustion, Turbulent Reacting Flows Shear Layers, Mixing, Mixing Enhancements, Laser Diagnostics Numerical Simulations, Stability Analysis				15. NUMBER OF PAGES 47	
				16. PRICE CODE	
17. SECURITY CLASSIFICATION OF REPORT Unclassified	18. SECURITY CLASSIFICATION OF THIS PAGE Unclassified	19. SECURITY CLASSIFICATION OF ABSTRACT Unclassified	20. LIMITATION OF ABSTRACT UL		

NSN 7540-01-280-5500

Standard Form 298 (Rev. 2-89)
Prescribed by ANSI Std. Z39-1
298-102

TABLE OF CONTENTS

1.0	SUMMARY.....	1
2.0	INTRODUCTION.....	1
3.0	STABILITY ANALYSIS OF FLOW STRUCTURE	2
3.1	Objective	2
3.2	Research Results	2
3.2.1	Explanation and Prediction of Flow Structure.....	2
3.2.2	Overview of the Parameter Space.....	3
3.2.3	Structural Regime Charts.....	8
4.0	DIAGNOSTIC TECHNIQUE DEVELOPMENT	9
4.1	Objectives	9
4.2	Research Results	10
4.2.1	Flow Facilities	10
4.2.2	PLIF Imaging of Shock Tunnel Transient	10
4.2.3	PLIF Imaging of Injector Flowfield.....	11
4.2.4	PLIF Thermometry in Underexpanded Free Jet	11
5.0	MIXING AND REACTION IN SUPERSONIC FLOW	17
5.1	Objectives	17
5.2	Research Results	17
5.2.1	Diagnostic Development	21
5.2.2	Compressible Mixing: Imaging Results	23
5.2.3	Compressible Mixing: Statistical Results	24
5.2.4	Mixing Enhancement.....	34
5.2.5	Mixing Enhancement Results: Images	34
5.2.6	Mixing Enhancement Results: Statistics	35
5.2.7	Mixing Enhancement Results: Quantitative Cold Chemistry Measurements	41
6.0	REFERENCES	42
6.1.	Publications.....	44
6.2.	Presentations	44
7.0	PERSONNEL	45
8.0	PH.D. DEGREES AWARDED	45

1.0 SUMMARY

An experimental and computational investigation of supersonic combustion flows has been carried out. The principal objective of the research was to gain a more fundamental understanding of mixing and chemical reaction in supersonic flows. The research effort comprised three inter-related elements: (1) stability analyses and numerical simulations of compressible reacting flows; (2) development of laser-induced fluorescence techniques for time-resolved multidimensional imaging of species concentration, temperature, velocity and pressure; and (3) an experimental study of mixing and combustion in a supersonic plane mixing layer with the additional development of simple mixing enhancements. The specific objectives and results of the research of each of these program elements are summarized in this report.

2.0 INTRODUCTION

Air-breathing propulsion systems offer the potential of higher performance than conventional rocket engines for hypersonic flight. To realize this potential, new combustor design concepts are required. In particular, in order to minimize losses associated with strong shock waves and high combustor inlet temperatures, it is desirable to maintain high flow velocities in the combustion chamber. This design concept leads to a new class of propulsion devices where combustion takes place in supersonic flow.

Combustion in supersonic flow is fundamentally different from combustion in the subsonic flow regime employed in all currently-operating aircraft engines. Many of the design approaches developed over the years for subsonic combustors, *e.g.*, ignition and flame stabilization techniques, are not applicable to supersonic combustion devices, and the current understanding of the fundamental aspects of supersonic combustion is inadequate to support development of these devices.

Recent advances in diagnostic capabilities and significant improvements in our ability to compute such flows offer new opportunities to obtain needed fundamental understanding of compressible turbulent reacting flows. To achieve this understanding, we have carried out a closely-coordinated experimental and computational program that utilized state-of-the-art experimental techniques and computational methods.

The principal objective of the research is to gain a more fundamental understanding of the flow physics and chemistry interactions in compressible turbulent reacting flows. The project comprised three inter-related efforts: (1) stability analysis

and numerical simulation of supersonic flows with mixing and chemical reaction; (2) an experimental study of mixing and combustion in supersonic flows with the additional development of simple mixing enhancements; and (3) development of laser-induced fluorescence techniques for time-resolved multidimensional imaging of species concentration, temperature, velocity and pressure in supersonic flows. A close coupling of these efforts was maintained in order to maximize our understanding of compressible turbulent reacting flows with an emphasis on supersonic combustion. The specific objectives and results of the research of each of the program elements are described in the following sections.

3.0 STABILITY ANALYSIS OF FLOW STRUCTURE

3.1 Objective

The objective of the numerical portion of the project has been to use stability analysis to gain insight into how the flow structure and physics of the compressible reacting mixing layer change within a parameter space defined by compressibility, heat release and the density, equivalence and velocity ratios.

3.2 Research Results

Previous simulations done by Planché and Reynolds (1992a,b) have demonstrated that a compressible reacting mixing layer can develop two instability modes in addition to the more common central mode that exists unaccompanied in incompressible non-reacting flows. These two additional modes are termed "outer" because of their association with the fast and slow free streams. These initial simulations demonstrated the adverse impact of an outer mode structure on the global reaction rate, and thereby motivated our interest to gain better insight into the range of flow conditions that result in the outer modes becoming the dominant instability.

3.2.1 Explanation and Prediction of Flow Structure

The density weighted vorticity profile ($\bar{\rho} d\bar{u}/dy$) provides an extremely useful tool for both describing and predicting the first order behavior of the mixing layer. A view of how this profile changes under the influence of increasing compressibility and heat release is shown in Figure 1. Our results parameterize the effect of compressibility with the convective Mach number, M_c , and the amount of heat release by a non-dimensional heat of reaction, Θ . This figure demonstrates that both combustion (through

heat release) and compressibility (through viscous heating) act to increase the temperature and correspondingly decrease the density along the centerline. This results in a fundamental change in the $\bar{\rho} d\bar{u}/dy$ profile from a single centrally located peak to a bimodal appearance for sufficiently large Θ and M_c values. This evolution suggests that the mixing layer will develop two additional instability modes—one associated with each of the fast and slow streams—that are distinct from the central mode, which itself is responsible for the familiar vortical structure found in incompressible, non-reacting situations.

The implications of this $\bar{\rho} d\bar{u}/dy$ change are presented in Figures 2 and 3. For the case of low compressibility and heat release shown in Figure 2, the single peaked $\bar{\rho} d\bar{u}/dy$ profile results in a flow structure that provides direct entrainment of fuel and oxidizer together. In contrast to this, when both compressibility and heat release are increased in Figure 3, the bimodal density weighted vorticity profile results in a two-step mixing process: the vortical structure of the fast mode mixes oxidizer into the reaction zone while the slow mode mixes in the fuel. Planché and Reynolds' simulations documented the adverse impact of this two-step process on the global reaction rate, implying a reduction in the mixing performance for the flow. Given this impact, there is significant interest in improving our understanding of how the structure of the mixing layer, and hence its mixing ability, changes as a function of the full parameter space.

3.2.2 Overview of the Parameter Space

An extensive, five-dimensional parametric study was conducted with a focus on determining which variables were most important in determining the flow structure. The results indicated that compressibility, heat release and density ratio ($s = \bar{\rho}_2/\bar{\rho}_1$) effects were the most important parameters in establishing the flow structure; the effect of the equivalence and velocity ratios were found to be less critical (Day et al. 1997b). A good appreciation for the effect of the three most important parameters can be developed by considering the evolution of the eigenfunction energy profile, $\hat{u}_i \hat{u}_i^* = \hat{u} \hat{u}^* + \hat{v} \hat{v}^* + \hat{w} \hat{w}^*$. To create a visualization that combines a view of both the distribution of vortical energy and the amplification rate, we define a new variable

$$\Psi = -\alpha_{i,\max} / (-\alpha_{i,\max,o}) \hat{u}_i \hat{u}_i^*$$

where the energy term $\hat{u}_i \hat{u}_i^*$ is calculated for the instability wave at the frequency and obliquity angle of the most amplified mode. The energy was normalized to have a maximum value of unity before being multiplied by the ratio of the amplification rate at

the position of interest ($-\alpha_{i,\max}$) to a reference amplification ($-\alpha_{i,\max,0}$). The reference chosen here is the canonical case of an incompressible, non-reacting, equal density mixing layer with $\bar{u}_2 = 0$.

The Ψ profile that corresponds to this reference condition is shown in Figure 4 as the first of three images that detail the influence of compressibility on the flow structure. There is only a single amplified mode at the reference condition and its wide and centrally located energy profile identifies it as the central mode. The broad distribution of energy in this case is the signature of the well understood large scale structure that directly mixes fuel and oxidizer together. As compressibility increases to $M_c = 1$ in Figure 4, the growth rate of the central mode drops and its energy distribution becomes slightly more compact. Also appearing at this compressibility, but at very low amplification rates, are the fast and slow outer modes. Consistent with the ideas presented in our $\bar{p} \, d\bar{u}/dy$ discussion, the results at $M_c = 2$ indicate that the growth rates of the outer modes strengthen relative to the central mode with increasing compressibility, but still remain secondary to the rate of the central mode at this M_c value.

The outer modes will dominate the flow structure when heat release effects become significant. This situation is documented in Figure 5 which shows the effect of increasing heat release relative to the non-reacting case at $M_c = 2$. A comparison between the eigenfunction energy profiles at $M_c = 2$, $\Theta = 0$ and $M_c = 2$, $\Theta = 1$ demonstrates that the introduction of heat release at this Mach number entirely stabilizes the central mode but destabilizes the outer modes. The nature of the two-step mixing process that was detailed in the DNS studies of Planché and Reynolds (1992a,b) is evident from the separate and distinct energy distributions shown in the $M_c = 2$, $\Theta = 1$ plot.

The influence of the density ratio on the flow structure is also seen in Figure 5. This sequence of energy profiles details the effect of a fast ($s = 0.5$) and slow ($s = 2.0$) side density bias relative to the equal density $M_c = 2$, $\Theta = 0$ case. Doubling the density on the fast side causes the fast and central modes to be nearly equally amplified, forming one variety of colayer structure in the flow, while the same change is observed to stabilize the slow mode. The increase in density on the fast side has also moved the position of all three vortical modes upwards in the layer. The profiles for a slow side density bias show the opposite result with this change causing the formation of a central/slow mode colayer and a general shift towards the slow side.

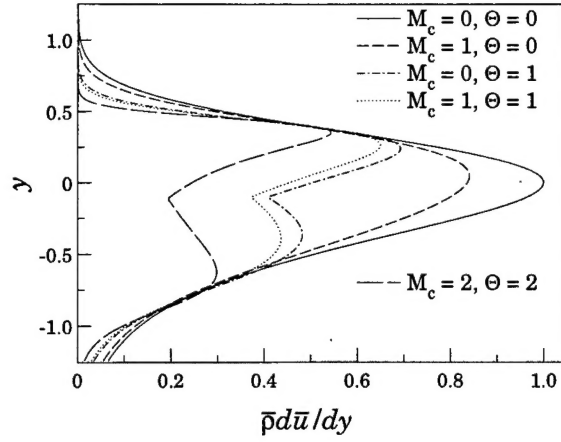


Fig. 1: Density weighted vorticity development with compressibility and heat release ($\bar{u}_2 = 0, s = 1, \phi = 1$).

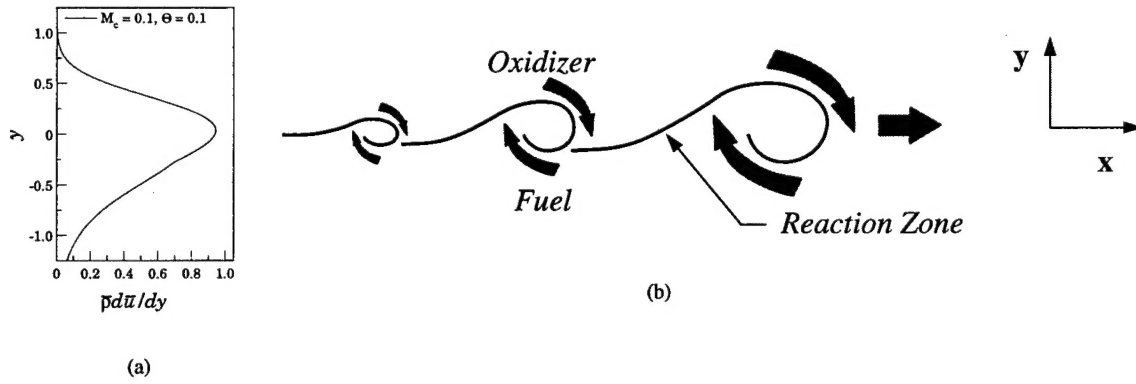


Fig. 2: Characteristics of a low compressibility, low heat release mixing layer at $\Theta = 0.1$ and $M_c = 0.1$: (a) density weighted vorticity profile (b) single step mixing process for this central mode flow structure.

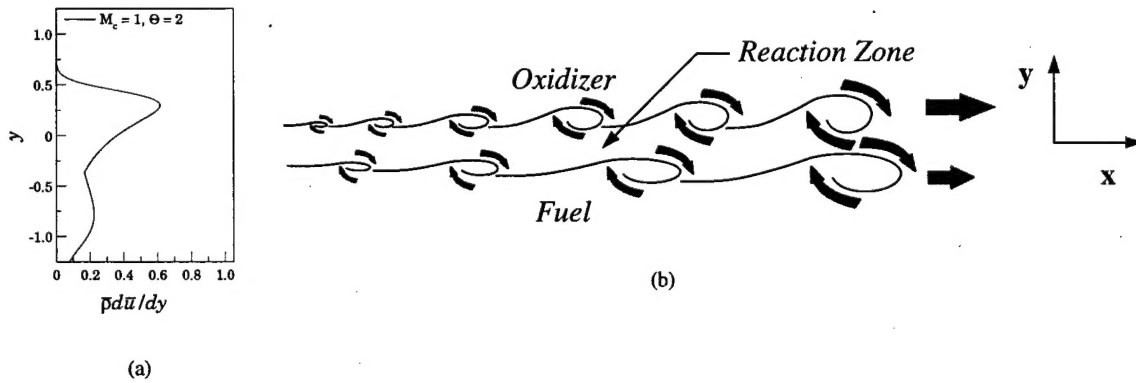


Fig. 3: Characteristics of fully compressible reacting mixing layer at $\Theta = 2.0$ and $M_c = 1.0$: (a) density weighted vorticity profile (b) two step mixing process for this outer mode flow structure.

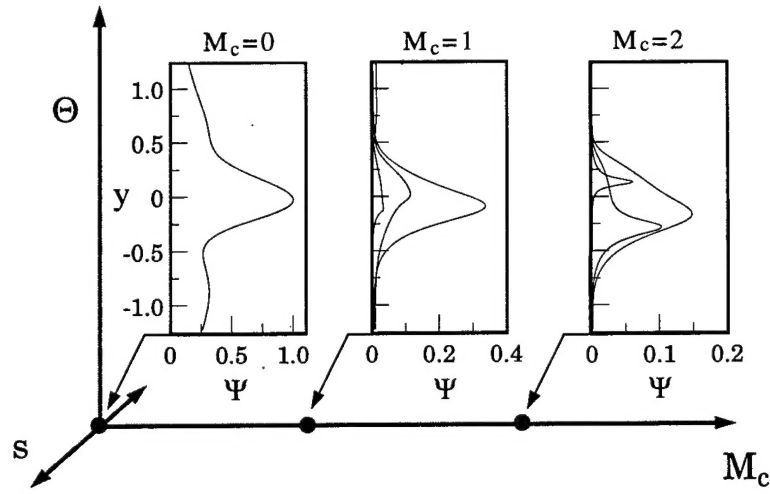


Fig. 4: Effect of compressibility on the amplification rate normalized eigenfunction energy profiles for each mode at $M_c = 0, 1$ and 2 ($\Theta = 0, \bar{u}_2 = 0, s = 1$).

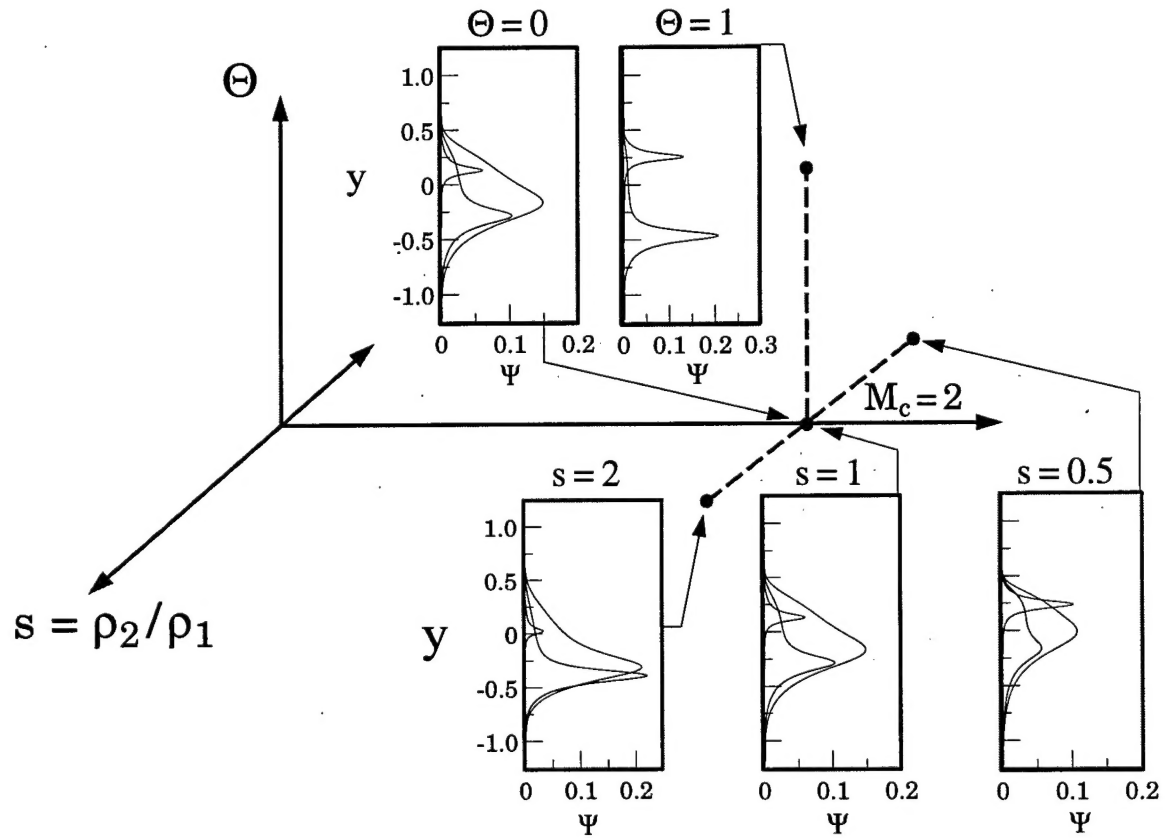


Fig. 5: Effect of heat release and density ratio variation on the amplification rate normalized eigenfunction energy profiles at high compressibility ($M_c = 2, \phi = 1, \bar{u}_2 = 0$).

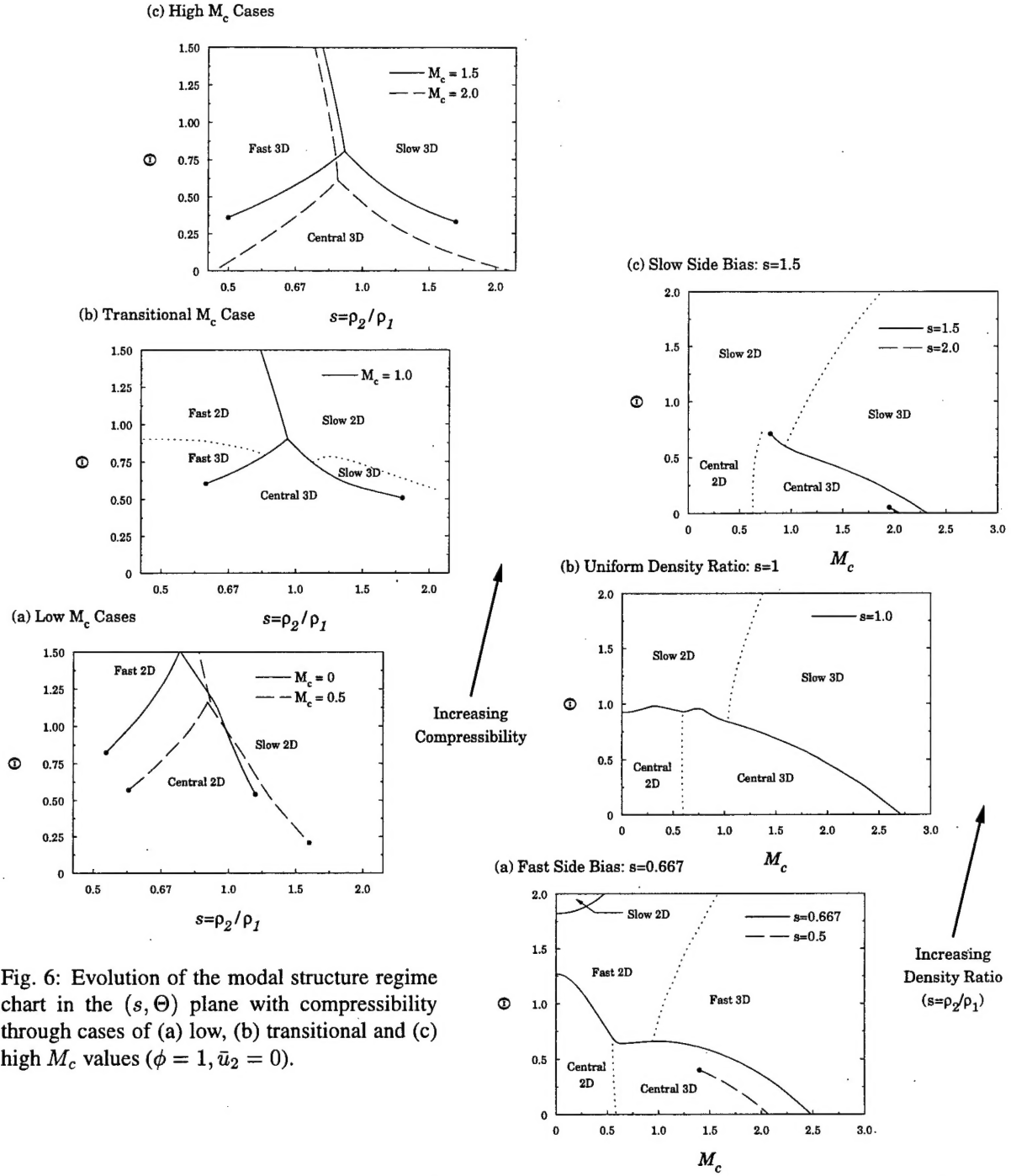


Fig. 6: Evolution of the modal structure regime chart in the (s, Θ) plane with compressibility through cases of (a) low, (b) transitional and (c) high M_c values ($\phi = 1, \bar{u}_2 = 0$).

Fig. 7: Evolution of the modal structure regime chart in the (M_c, Θ) plane with density ratio value increasing through cases of (a) $s = 0.5$, (b) $s = 1$ and (c) $s = 2$ ($\phi = 1, \bar{u}_2 = 0$).

3.2.3 Structural Regime Charts

A more complete understanding for the interaction of the three dominant parameters (M_c , Θ , and s) can be developed by taking two-dimensional cuts through the parameter space to investigate regions where specific modes will dominate. A series of these regime charts are presented in Figures 6 and 7 for cuts in the (s, Θ) and (M_c, Θ) planes, respectively.

The first point of interest concerns the shape of the colayer boundaries for low M_c values in (s, Θ) plan of Figure 6(a). The evolution of the $\bar{\rho} d\bar{u}/dy$ profile toward two outer peaks with higher heat release is reflected in the progression of the regime chart from a central to outer mode structure with increasing Θ . Also, the correlation of regions where an outer mode (fast or slow) dominates with regions where their companion streams have greater density follows from predictions based on the $\bar{\rho} d\bar{u}/dy$ profile. The wedge shape of the central mode region in Figure 6(a) can be explained from our earlier observations from the eigenfunction energy profile. The effect of increasing heat release to stabilize the central and destabilize the outer modes is reflected in the diminishing density ratio range where the central mode dominates as heat release is increased; the outer modes require less bias in the density ratio value to match the central mode amplification as the Θ value rises. The conditions of particular interest in this regime chart are the locus of points that form the boundaries between modes. For these conditions, the flow will develop two vortical modes that contribute to the mixing of the fast and slow streams and therefore hold promise for enhanced mixing performance.

Shifting focus now to the results at $M_c = 0.5$ that also appear in Figure 6(a), we see that the predominant features of the previous chart remain unchanged but here the outer modes occupy a larger region. This follows directly from the fact that both compressibility and heat release generate conditions where outer modes dominate the structure. Further increases in M_c are pictured in Figures 6(b) and (c) and they show a continuation of the trend toward outer mode domination and three-dimensionality for all modes. Indeed, at $M_c = 2$ it becomes possible to maintain a colayer structure in non-reacting flow, provided the density ratio is carefully chosen.

Figure 7 offers a perspective from the (M_c, Θ) plane for a variety of density ratios. These planar cuts allow discussion of the mixing layer development from the reference condition of an incompressible, non-reacting case (located in the lower left corner) to a fully compressible reacting flow over a range of fixed density ratios. It is useful to start

the discussion with the reference case of $s = 1$ that is shown in Figure 7(b). Under the conditions of $M_c = 0$ and $\Theta = 0$ the familiar, centrally located, two-dimensional, large scale structure will be present and dominant. With increasing compressibility there is first a transition to three dimensionality and then, for $M_c > 2.5$, the central mode gives way to the slow three-dimensional mode as the dominant flow structure. With increasing heat release the progression from central to slow mode structure is again observed. At this unity density ratio value the slow mode will slightly out-pace the fast and it dominates the regions of both high compressibility and heat release.

For the case of a fast side density bias of $s = 2/3$ pictured in Figure 7(a), the central/outer mode colayer boundary maintains the same characteristics as in the $s = 1$ case but here the fast mode replaces the slow as the dominant outer structure over most of the considered regime. The $s = 1/2$ case also shown in Figure 7(a) demonstrates that colayer regions are almost entirely eliminated at this level of density bias. Therefore, there will only be one discernible mixing mode in the flow for the vast majority of this parameter plane. When the density bias is moved to the slow side of the layer in Figure 7(c), the location of the central/slow colayer drops in both M_c and Θ values and also reduces in length compared to the equivalent density case of Figure 7(b). When the density ratio is increased further to $s=2$, the colayer boundary is all but eliminated.

4.0 DIAGNOSTIC TECHNIQUE DEVELOPMENT

4.1 Objectives

Over the past several years, investigators in our laboratories have pursued the development of laser-based diagnostic techniques applicable in the pulsed flow facilities frequently used in ground-based testing of high-speed aerodynamic and propulsion concepts. Our efforts have focused on PLIF imaging, which is particularly attractive because it can yield species- and quantum-state-specific data with high temporal and spatial resolution, excellent background rejection, and low noise. The use of PLIF in transient, high-speed flows was pioneered at Stanford and workers in our laboratories were able to demonstrate essentially instantaneous measurements of rotational and vibrational temperature and velocity fields.

4.2 Research Results

4.2.1 Flow Facilities

The small-scale facility shown schematically in Fig. 8 was constructed to provide inexpensively a controlled environment for PLIF diagnostic development. The facility may be operated either as a shock tube or as a reflection-type shock tunnel (with a rapid conversion procedure) and may be used to create a variety of supersonic flowfields. A wide range of operating conditions is available for tests in the facility. Figure 9 illustrates the shocked-gas pressure and temperature in the driven section as a function of initial test gas pressure for a typical driver-gas condition. Usually, the test gas is composed of an inert gas (*i.e.*, Ar or N₂) seeded with a small mole fraction of a fluorescent species (NO) or with reactants that form a fluorescent species (OH) following shock-heating. Alternatively, NO- or reactant-bearing gas may be introduced through a wall-mounted injector. The duration of steady flow conditions varies inversely with the enthalpy of the flow and ranges from ~150 μ s to 1.5 ms.

The basic optical arrangement used in acquiring PLIF images is illustrated in Fig. 8. Frequency-doubled photons from a tunable, excimer-pumped dye laser are formed into a sheet ~50 mm wide and 0.2–0.4 mm thick and directed across the midplane of the test section through a UV-grade fused silica window. During each run of the facility, a single laser pulse, fired at the desired moment of observation, excites an isolated rovibronic transition of the tracer species present in the flowfield. A fraction of the resulting fluorescence burst is imaged onto a gated, intensified charge-coupled device array mounted perpendicular to the laser sheet. Spectral filtering is used to eliminate detection of luminosity from the flow as well as fluorescence resonant with the laser frequency and direct laser scattering from walls and windows. The captured PLIF image is then transferred to computer for further analysis and display.

4.2.2 PLIF Imaging of Shock Tunnel Transient

Figure 10 shows the results of a series of experiments in which PLIF imaging of NO was used to examine the evolution of the flow up- and downstream of the shock-tunnel nozzle (Palmer and Hanson, 1995). The images provide midplane views of the reservoir and jet flowfields at different delays with respect to the time at which the incident shock reached the endwall. The initial distortion of the reflected shock due to the nozzle entrance in the endwall and the resultant perturbations in the reservoir are observable. The process of jet

startup to a quasi-steady flow condition, including the bursting of the diaphragm placed at the nozzle exit and its passage through the downstream imaged region, is illustrated as well. At long delay times, disturbances arriving from upstream altered the pressure and temperature of the gas, thereby terminating the period of stable reservoir conditions. These images not only allow a detailed examination of the flow physics, but also provide crucial information about the operating characteristics of the shock tunnel.

4.2.3 PLIF Imaging of Injector Flowfield

Because the PLIF signal is a complex function of temperature, pressure, and gas composition, the interpretation of an individual image is often difficult. However, analysis of two or more PLIF images of a flowfield can yield a specific flow property, such as temperature or velocity. For instance, investigators in our laboratory have used two complete laser/camera systems in the acquisition of temporally-resolved and mean rotational temperature fields in a model SCRAMJET injector flowfield (McMillin *et al.*, 1994), as shown in Fig. 11. The lasers were tuned to two transitions originating from different rotational states within the lowest vibrational level of NO or OH. A brief time period between the firing of the two lasers allowed each camera to integrate the signal induced by only one of the lasers, while capturing the flowfield with flow-stopping temporal resolution. The rotational temperature, assumed to be identical to the translational temperature, was inferred from the ratio of the two signals on a pixel-by-pixel basis. A comparison of the results obtained with PLIF of NO and OH illustrates the complementary nature of the two techniques and, in the region of overlap, validates each of the mean temperature measurements.

4.2.4 PLIF Thermometry in Underexpanded Free Jet

An NO PLIF thermometry technique has also been applied in a highly underexpanded free jet created at the exit of a converging nozzle (Palmer *et al.*, 1996). The results of these experiments are shown in Fig. 12. Whereas previous rotational temperature measurements were performed in flows with shock waves, the focus in this experiment was on application in a high-speed flow with yet more extreme temperature and pressure variations. The method used was similar to that described above, although only one PLIF image was acquired during each run of the facility. Because the flow was laminar and reproducible, temporal resolution was not required, except insofar as each image had to be captured during its brief, quasi-steady period, which made necessary the use of a single-shot imaging technique. PLIF images acquired by pumping transitions originating

from four different rotational states were combined to yield the mean temperature field in the free jet. The temperature inferred from single-shot and frame-averaged PLIF images agrees well with the results of a simulation of the flowfield by the method of characteristics.

The examples of PLIF results provided here demonstrate the frame-on-demand capability crucial for imaging experiments in impulse flow facilities as well as some of the flow property measurement strategies developed in our laboratory. Other applications of PLIF imaging of NO in the shock tube/tunnel facility have included: visualization of the establishment of bow shocks over blunt bodies placed in the shock tube (McMillin *et al.*, 1991) and at the exit of a converging-diverging shock-tunnel nozzle (Houwing *et al.*, 1996) along with rotational thermometry in the resulting quasi-steady flows, vibrational thermometry across planar shock waves (McMillin *et al.*, 1989) and in free jets with vibrational nonequilibrium (Palmer and Hanson, 1993a), and temporally-resolved, two-component velocimetry in a free jet flow (Palmer and Hanson, 1993b). In addition, PLIF imaging of OH has been applied to measurements in a variety of reacting, high-speed flowfields, including: temporally-resolved rotational thermometry in planar shocks (Seitzman *et al.*, 1994) and in bow shock flows (Seitzman and Hanson, 1993), visualization of the development of a free jet of combustion product gases (Palmer and Hanson, 1995), and mean rotational thermometry in the resulting quasi-steady flowfield (Palmer and Hanson, 1996).

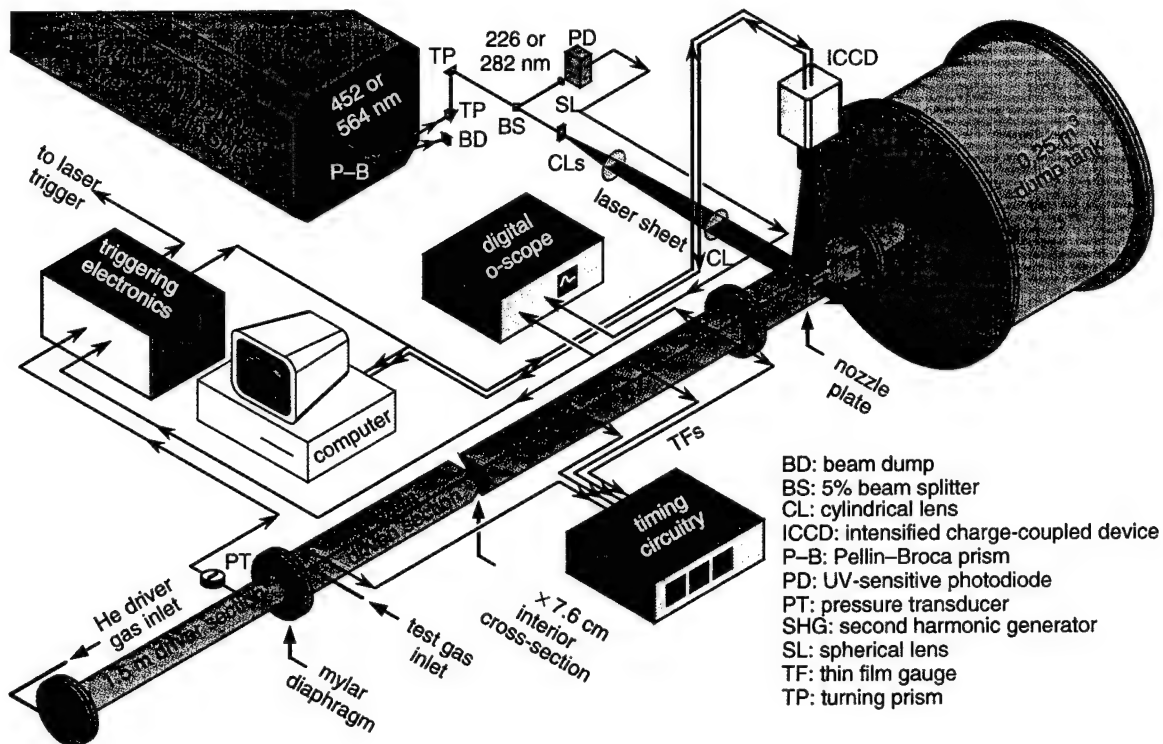


Fig. 8. Shock tube/tunnel facility with associated optical and electronic components for PLIF imaging. In the configuration shown, the facility is operated as a reflection-type shock tunnel; for operation as a shock tube, the nozzle plate, located at the end of the driven section, is replaced with a solid endwall.

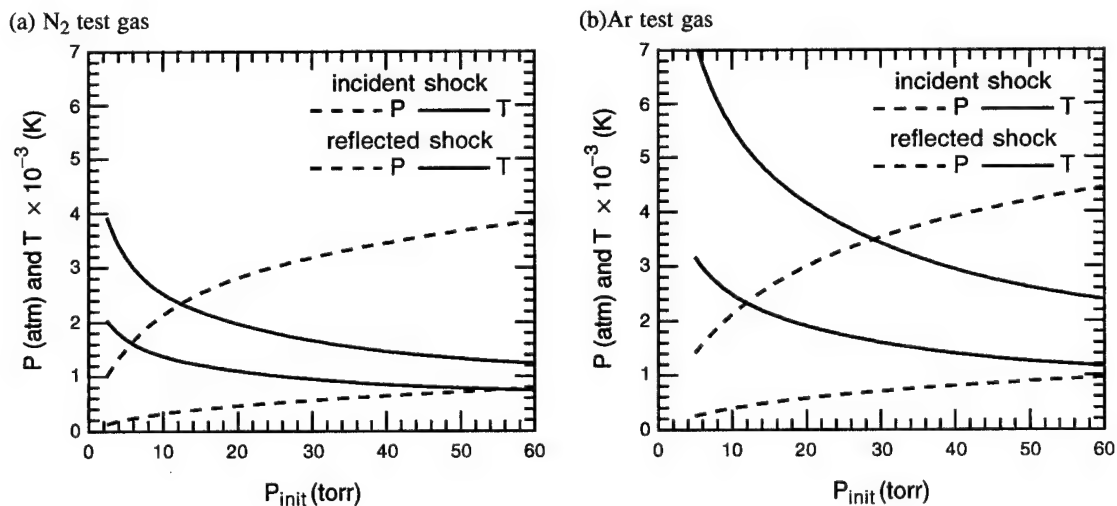
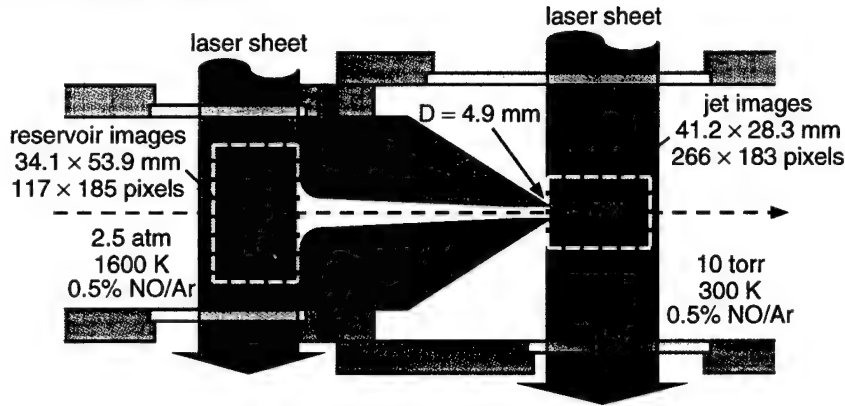


Fig. 9. Shock tube performance characteristics with an initial driven-section loading of (a) N₂ or (b) Ar at pressure P_{init} and 300 K for a single driver-gas condition (*i.e.*, room-temperature He at 3.4 atm, with a 10-mil-thick mylar diaphragm). The pressure (P) and temperature (T) behind the incident and reflected shocks were calculated using incident shock speeds measured at various P_{init} .

(a) test section midplane



(b) NO PLIF imaging results

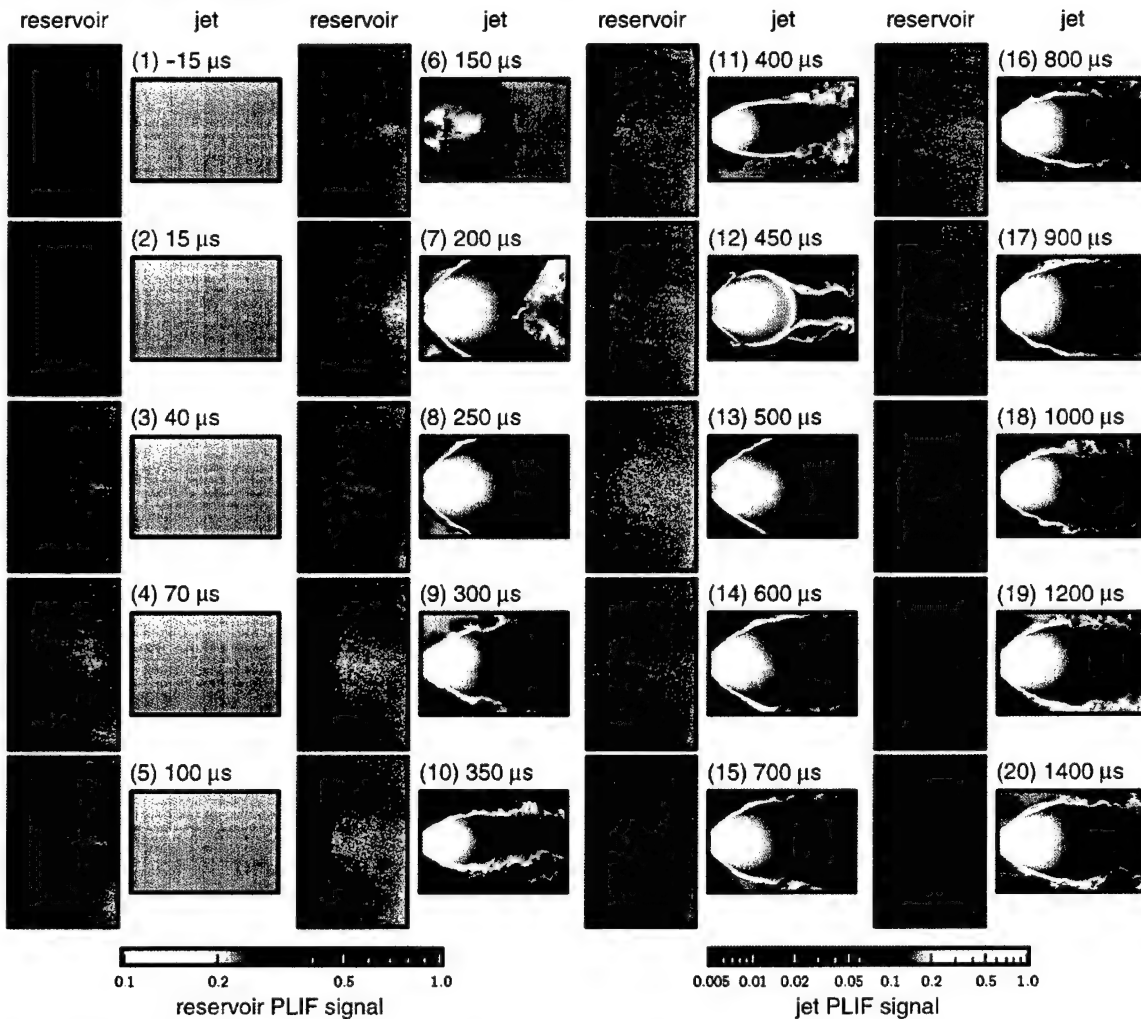
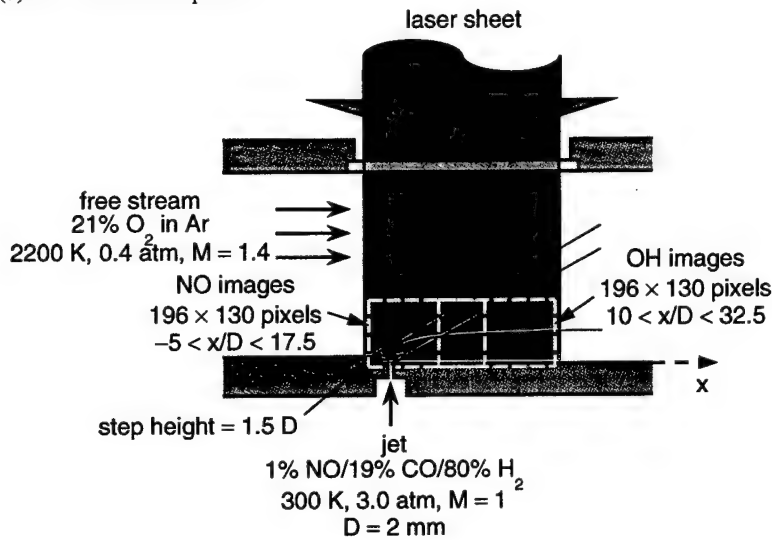


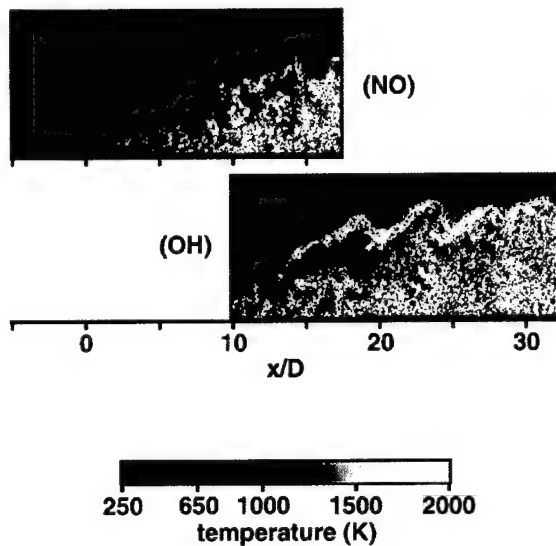
Fig. 10. PLIF imaging of the shock-tunnel flow transient. The locations of the two imaged regions (*i.e.*, reservoir images and jet images) are illustrated in (a), which shows the test section midplane viewed from above and gives the nominal conditions in the reservoir and far downstream of the nozzle. Each NO PLIF image in (b.1–20) was acquired at the delay times listed with it (with respect to the time of incident shock reflection). The sequences illustrate the process of shock reflection, the development of the free jet flowfield, and the establishment and duration of steady flow conditions.

(a) test section midplane



(b) NO and OH PLIF thermometry results

(1) single-shot



(2) frame-averaged

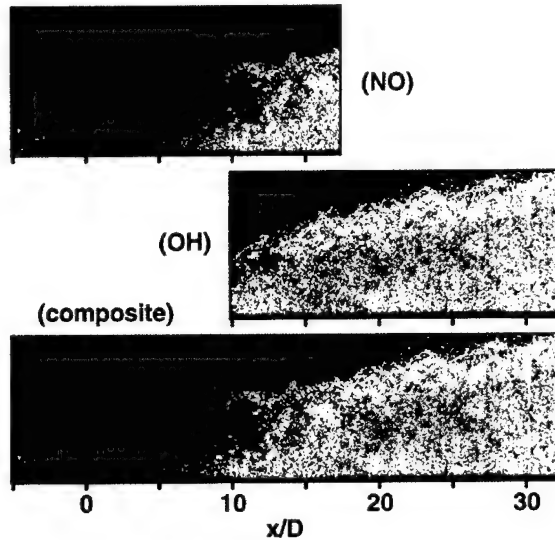
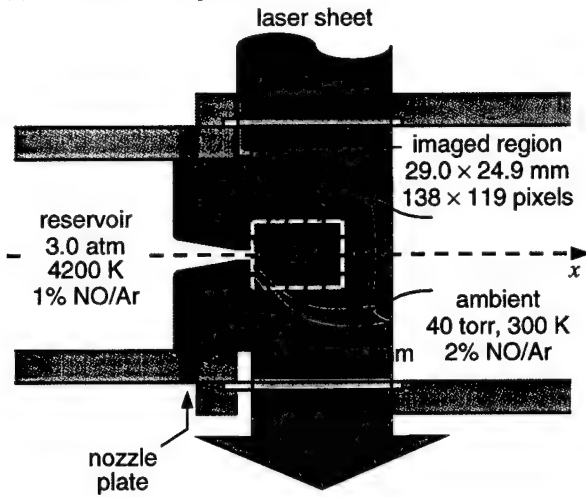


Fig. 11. PLIF thermometry in a model SCRAMJET injector flowfield. The test section midplane, viewed from above, is shown in (a) to illustrate the locations of the imaged regions (*i.e.*, NO images and OH images) with respect to the step in the side wall and the jet-injection port. The images in (b.1) are temporally-resolved temperature fields acquired with PLIF of NO and OH, as labeled. The images in (b.2) are mean temperature fields constructed by frame-averaging individual images of the type shown in (b.1). Six single-shot images were used for NO and twelve for OH in (b.2). Also shown is a composite image constructed from the mean NO and OH temperature images. The scale located at the bottom of (b.1) gives the relationship between the displayed color and the rotational temperature in the images.

(a) test section midplane



(b) NO PLIF thermometry results

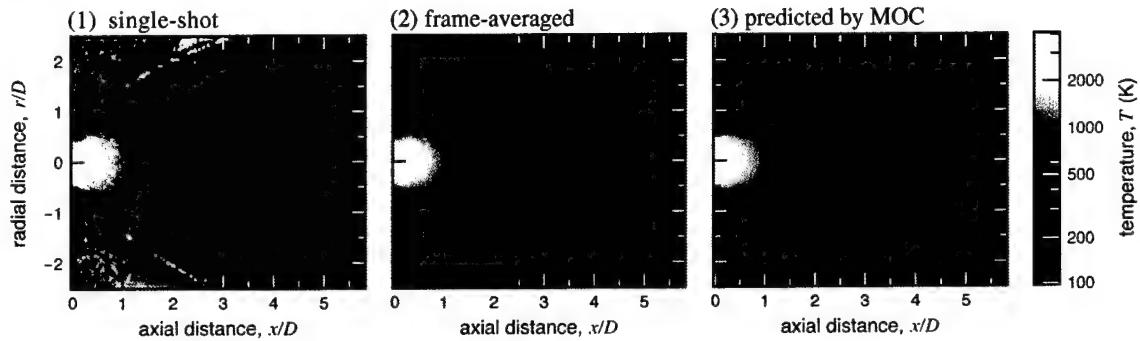


Fig. 12. Multi-line PLIF thermometry in a shock-tunnel free jet. The test section midplane, viewed from above, is shown in (a) to illustrate the location of the imaged region. Shown in (b) are temperature fields inferred from (1) single-shot and (2) frame-averaged PLIF images. The temperature predicted by a method-of-characteristics simulation of the free jet is given for comparison in (b.3).

5.0 MIXING AND REACTION IN SUPERSONIC FLOW

5.1 Objectives

The objectives of this part of the program are (1) the experimental study of mixing and chemical reaction in a compressible mixing layer and (2) investigation of mixing enhancement in supersonic shear layers. The data acquired, using conventional and laser-based diagnostics, provide important new insights into mixing and reaction processes under compressible conditions.

5.2 Research Results

In the primary experiments, the convective Mach number was varied from $M_c = 0.25$ to 0.75 , spanning the range from low to moderately high compressibility, and the influence on molecular-level scalar mixing measured with the relatively new cold chemistry planar laser-induced fluorescence technique. The technique provided a resolution-insensitive measurement of pure fluid from which the time-averaged probability of mixed fluid, shear layer mixing efficiency, mixed fluid composition, and other scalar quantities were derived from flip experiments where the constituent gases of each stream are exchanged. More traditional passive scalar PLIF measurements were also made to determine the mean composition profile and visualize the mixture fraction field.

In a secondary set of experiments, the use of boundary layer disturbances on the high-speed splitter tip was examined as a means to enhance mixing with low pressure loss. The shape, number, obliquity, offset, and thickness of the disturbances were parametrically varied and the qualitative effect on mixed fluid visualized with planar laser Mie scattering. For the most promising geometry, quantitative measurements were made using the cold chemistry mixing diagnostic.

Key results from the 1) diagnostic development effort, 2) influence of compressibility on scalar mixing, and 3) mixing enhancement studies are summarized below. The complete findings of this work are described in the Ph.D. dissertation of T. Island (1997).

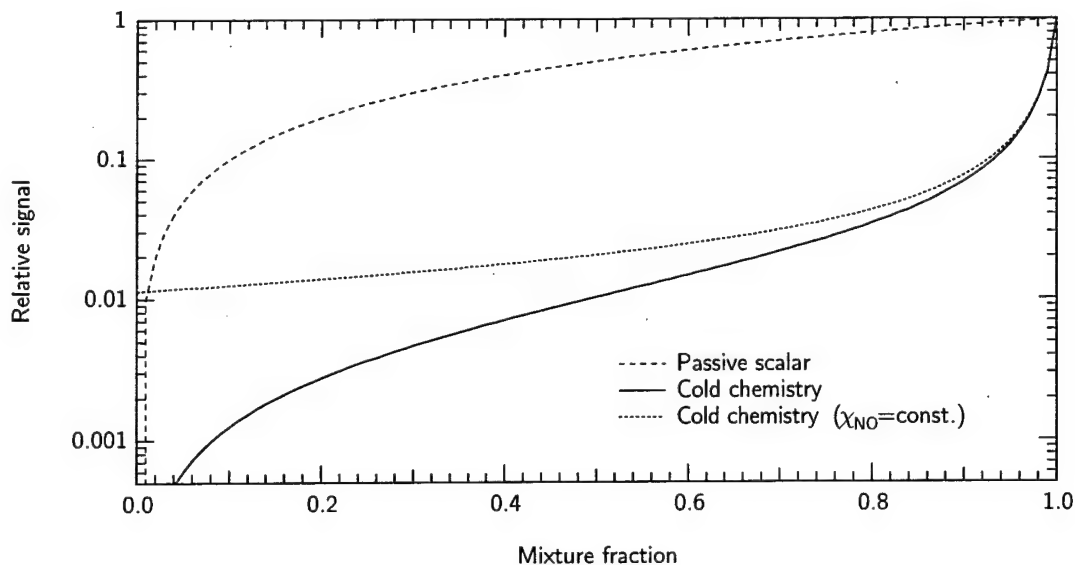


Fig. 13. Calculation comparing the cold chemistry and passive scalar signals. The seeded high-speed stream ($\xi = 1$) is N_2 and the unseeded stream is air. The calculation is performed with $P = 10$ psia, $T_1 = 150$ K and $T_2 = 290$ K, matching the high-compressibility experimental conditions and assumes $1/A_{21} = 202$ ns, $\sigma_{N_2} = 0.01 \text{ \AA}^2$ and $\sigma_{O_2} = 25 \text{ \AA}^2$.

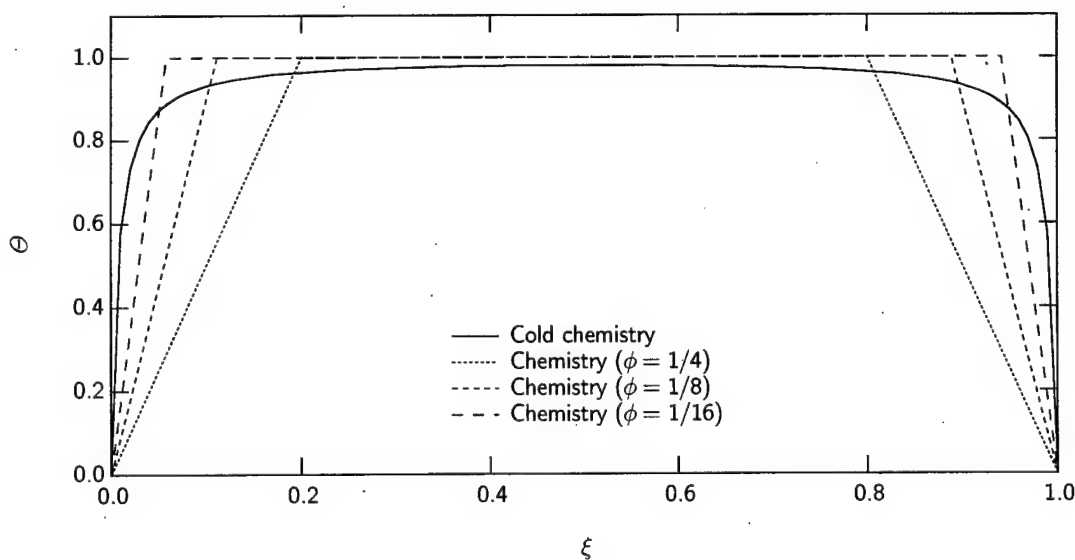


Fig. 14. Transfer function Θ for cold chemistry and chemical reaction methods displaying the sensitivity of the techniques.

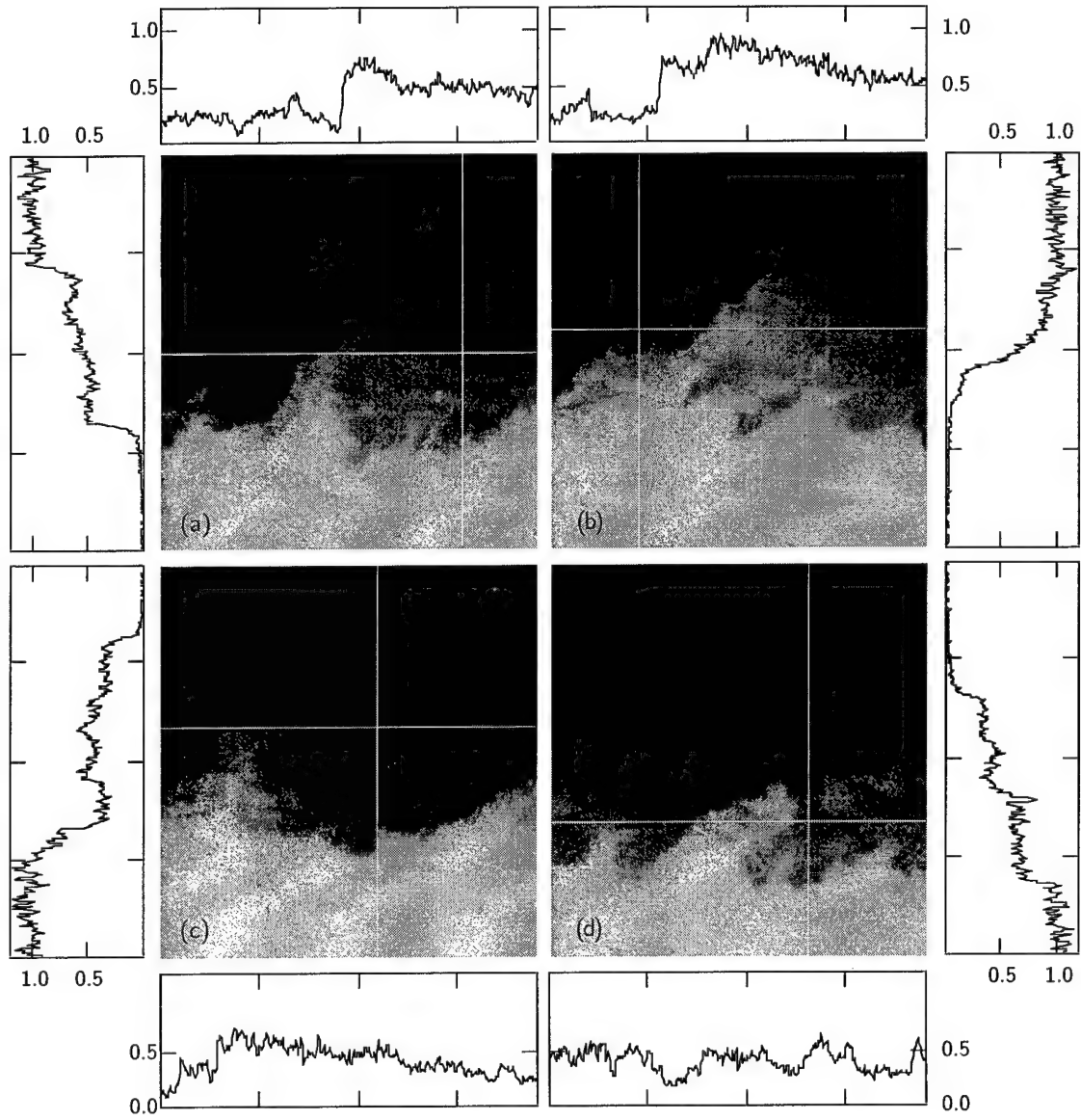


Fig. 15. Magnified passive scalar images at $M_c = 0.39$ with slow-side seeding. Flow is left-to-right with the high-speed stream on top and the imaged region is $\Delta x = 4.8$ cm by $\Delta y = 5.0$ cm. Plotted is the low-speed mixture fraction ξ_2 versus distance along the streamwise and transverse lines indicated.

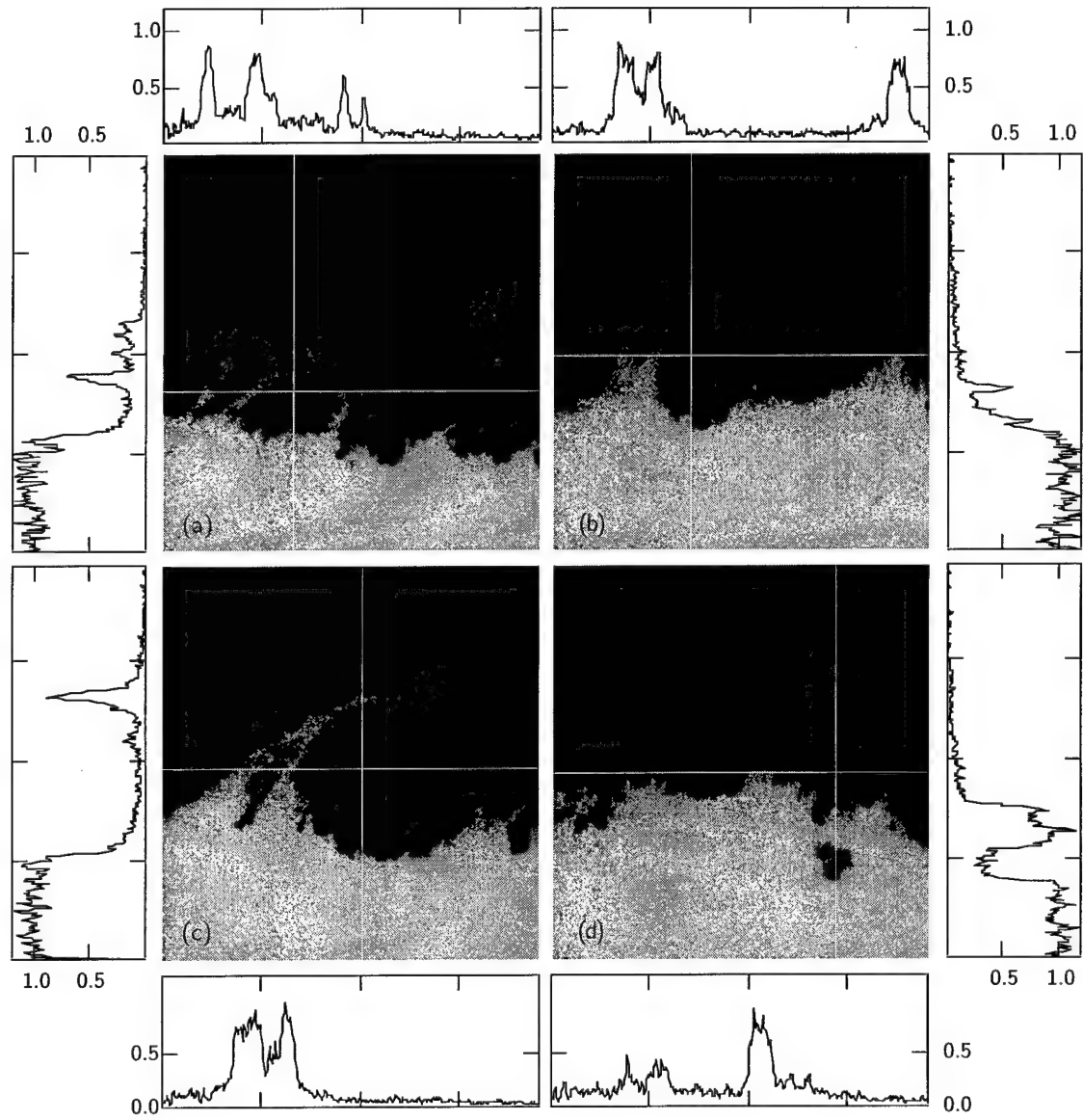


Fig. 16. Magnified cold chemistry images at $M_c = 0.39$ with slow-side seeding. Flow is left-to-right with the high-speed stream on top and the imaged region is $\Delta x = 4.8$ cm by $\Delta y = 5.0$ cm. Plotted is the pure fluid fraction versus distance along the streamwise and transverse lines indicated.

5.2.1 Diagnostic Development

Since the cold chemistry technique used to quantitatively measure molecular mixing is relatively new (Paul and Clemens (1993); Clemens and Paul (1995)), diagnostic development was an important aspect of this work. In this method, NO is seeded in a nitrogen stream that mixes with an unseeded air stream. Fluorescence from the seeded fluid will be strongly quenched by oxygen for fluid that has been mixed. The quenching occurs by molecular collisions in a time scale of tens of nanoseconds compared to the microsecond fluid mechanical time scale, thus mimicking a very fast, fuel lean chemical reaction without the complication of heat release. Because even a small amount of air reduces the fluorescence below detection, the signal is approximately binary, being high for pure fluid and low for mixed fluid. Therefore, even though the probe (pixel) volume may be significantly larger than the smallest scales of mixing, the cold chemistry method returns the fraction of pure seeded fluid present in the probe volume. Quantitative statistical mixing quantities can be derived from flip experiments measuring these pure fluid profiles. The current work extends the technique by combining passive scalar and cold chemistry methods to quantitatively determine the mixed fluid composition.

Extension for Mixed Fluid Composition

In a novel extension to the cold chemistry method, the mixed fluid composition ξ_m can be determined if cold chemistry and passive scalar measurements are combined. By definition, the mean high speed composition is

$$\bar{\xi}(\eta) = P_1(\eta)(1) + P_2(\eta)(0) + P_m(\eta)\xi_m.$$

where $\bar{\xi}$ is the mean high-speed mixture fraction, η is the transverse coordinate, P_i is the probability of pure fluid from stream i , P_m is the probability of mixed fluid, and ξ_m is the mean composition of the mixed fluid. Rearranging gives the expression for the mixed fluid composition

$$\xi_m(\eta) = \frac{\bar{\xi}(\eta) - P_1(\eta)}{P_m(\eta)}$$

where the mean composition $\bar{\xi}$ is determined by the passive scalar method and the pure fluid P_1 and mixed fluid profiles P_m are determined by the cold chemistry method. Essentially, the contribution of pure fluid to the mean is subtracted, leaving only the contribution of mixed fluid.

This extension to the cold chemistry measurement is significant since the mixed fluid composition and its distribution in the mixing layer is critical to many applications, such as supersonic combustion.

Signal Modeling

As described in Island (1997), a simple two-level model was developed for weakly and strongly quenched NO fluorescence and was used to estimate the theoretical accuracy of the cold chemistry method and compare the technique to chemistry-based mixing diagnostics. Figure 13 shows the complete normalized fluorescence signal for the passive scalar and cold chemistry methods as a function of high-speed mixture fraction when the seeded high-speed stream is N_2 and the unseeded stream is air. The passive scalar signal decreases linearly with mixture fraction due simply to dilution. The cold chemistry signal decreases non-linearly due to quenching, dominant at high mixture fractions, and linearly due to dilution, dominant at low mixture fractions. This can be seen by comparing the cold chemistry signal with the curve for constant mole fraction of NO as if both streams had been seeded. Because of the strong quenching, the signal is reduced ten-fold for 6% mixing, twenty-fold for 14% mixing, and 100-fold for 50% mixing.

Accuracy and Comparison to Chemical Reaction Techniques

The accuracy of the cold chemistry method can be examined using a mixed fluid transform function. From the PDF of mixture fraction, the probability of mixed fluid at any composition is defined as

$$\theta_m(y) = \int_{\epsilon}^{1-\epsilon} P(\xi, y) d\xi$$

where the arbitrarily small number ϵ indicates that contributions from pure fluid from either stream are excluded. We can introduce a transfer function θ representing the measurement technique such that

$$\theta_m(y) = \int_0^1 \Theta(\xi) P(\xi, y) d\xi$$

The estimate of mixed fluid θ_m will be quite good for transfer functions that approach the ideal: zero at $\xi = 0, 1$ and unity elsewhere. This function is plotted in Figure 14 along with the transfer function for the chemical reaction method.

The cold chemistry technique compares favorably with the chemical reaction approach for practical ϕ . One measure of comparison is the integral of the transfer function which equals 0.93 for cold chemistry and 0.80, 0.89, and 0.94 for $\phi = 1/4, 1/8$, and $1/16$ chemistry. Thus as a guide, the cold chemistry sensitivity is equal to the

chemical reaction method with $\phi = 1/16$. The absolute error depends on the actual distribution of mixture fractions, i.e. the PDF of mixture fraction. Using the incompressible data of Frieler (1992), the cold chemistry absolute errors are estimated to be roughly 15% at the edges and 5% near the center, always overestimating pure fluid. By comparison, the chemistry method with $\phi = 1/4$ underestimates the amount of mixed fluid by 40%, 7%, and 9% for $y/\delta = -0.4$, -0.2 , and 0 , respectively. At the edge of the layer the significant amount of mixed fluid near the freestream composition is missed at this low equivalence ratio.

5.2.2 Compressible Mixing: Imaging Results

PLIF images were acquired at four compressibilities ($M_c = 0.25, 0.39, 0.63$, and 0.76) and three Reynolds numbers for each compressibility except the highest, for a total of 10 cases. Four passive scalar images are shown in Figure 15 for slow-side seeding at $M_c = 0.39$, with horizontal and vertical lines indicating the location of the streamwise and transverse intensity “cuts” plotted adjacent to each image. Since these are quantitative images, the intensity scale represents mixture fraction ξ_i of seeded fluid. Images (a), (b), and (c) are clear examples of Brown-Roshko type rollers. As seen in the intensity profiles, the structures are often “ramped” in ξ in the streamwise direction and fairly uniform in the transverse direction. This is evidence of entrainment occurring by 2D motions with the structure core being biased in mixture fraction to the side from which it entrains pure fluid. For the images shown, the mixture fraction in the roller core is about $1/2$, but structure-to structure variation and streamwise ramping result in a smooth time-average.

Figure 16 shows typical cold chemistry images for the same low compressibility case. The seeded low-speed stream is nitrogen and the high-speed stream is air so that significant fluorescence quenching occurs in the mixed fluid by oxygen molecules. The cold chemistry images are nearly binary, with the pure seeded fluid white and mixed fluid black, in contrast to the many gray levels in the passive scalar images of Figure 15. In general, the 2D structure of the layer is harder to distinguish from the pure fluid images. As expected, however, many of the images (*e.g.*, (b) and (c)) strongly suggest that pure fluid from stream 2 is entrained on the upstream edge of the 2D roller (the tongues of pure fluid) and is well mixed in the roller core. As seen in the intensity cuts, transverse profiles though the mixing layer in regions not associated with presumed 2D structure, such as Figure 16 (d), show a rapid fall-off in the pure fluid with transverse distance. There is a relatively sharp interface between pure and mixed fluid in these regions and

the mixing layer contains very little pure fluid. However, even in these regions, a thin band of low signal (about 10%) along the pure fluid interface can just be discerned in the images and clearly seen in the transverse intensity profiles. This "halo" is most likely pure fluid present at scales below the resolution of the imaging system. From the halos, we assume that pure and mixed fluid is being stirred by the action of small-scale turbulence along the interface.

The following conclusions regarding the effects of compressibility may be generalized from the entire image set:

- 1) As seen by previous researchers, the passive scalar visualizations show a change in large-scale structure with increased compressibility. While somewhat variable, the low compressibility image sets are dominated by two-dimensional rollers exhibiting streamwiseramping and cross-stream uniformity in mixture fraction. At the higher compressibilities, the large-scale structure is highly variable with very few images exhibiting strongly two-dimensional structure.
- 2) Similarly, the cold chemistry visualizations of pure fluid indicate a change in structure with compressibility. At low compressibility, "tongues" of pure fluid appear to correspond with entrainment of high- and low-speed pure fluid along the leading- and trailing-edges, respectively, of two-dimensional structures and extend deep into the mixing layer. With higher compressibility, the pure fluid intrusions are less periodic and have a reduced transverse extent, indicating that entrainment is less two-dimensional.
- 3) The cold chemistry images frequently show a "halo" of low-signal signal level adjacent to pure fluid regions. In the low compressibility case, such regions extend well into the mixing layer and can be found in the (presumed) core regions of two-dimensional structures. At higher compressibility, the halo regions are, in general, less prevalent and more confined to the mixing layer edge.

5.2.3 Compressible Mixing: Statistical Results

Mean Composition

The profiles of mean composition or high-speed mixture fraction ξ vs. the normalized transverse coordinate, η , are shown in Figure 17. The $M_c = 0.63$ and 0.79 passive scalar results are corrected for air contamination and should be interpreted cautiously due to the uncertainty associated with the correction. The profiles of Figure 17 show fairly strong collapse to a single-inflection point profile. No clear trend with M_c or Re is evident within the uncertainty of the measurement, and we conclude that $\xi(\eta)$ is

not strongly influenced by compressibility in the range studied. In the present work, the mixing layer scalar thickness δ is defined as the transverse distance between the 5 and 95% points of the mean composition profiles ξ . In agreement with numerous studies, there is a strong decrease in mixing layer thickness normalized by its incompressible value at the same density and velocity ratio with increased compressibility.

Pure Fluid

The probability of pure seeded-side fluid $P_1(\eta)$ and $P_2(\eta)$ is plotted in Figure 18. This quantity is the normalized mean fluorescence signal of the cold chemistry flip experiments. The measurements indicate that the pure fluid transverse profiles, when scaled on η_{cc} based on the cold chemistry measurements themselves, are independent of Reynolds number and compressibility, strongly collapsing to a single-inflection point curve.

The pure fluid profiles are, however, shifted and stretched with respect to the mean composition (passive scalar) midpoint and thickness. To demonstrate, Figure 19 displays the probability of pure fluid versus η based on the corrected passive scalar profiles. In Figure 19(a), the probability of high-speed fluid at a given transverse location is seen to decrease strongly with compressibility. No such effect is indicated in Figure 19(b) along the low-speed interface for the low-speed fluid. Thus, we expect that the mean mixed fluid composition will be somewhat higher along the high-speed interface and relatively unchanged along the low-speed interface with increased compressibility.

Since instantaneous images were acquired, the root mean square (RMS) fluctuations in the pure fluid profiles $P_i(\eta)$ can be calculated. Figure 20 shows two interesting trends with increased compressibility: 1) the peak fluctuations shift towards the edges of the mixing layer for both P_1 and P_2 , and 2) the fluctuation peak narrows, mostly on the high-speed edge. Additionally, the fluctuation peak is generally broader along the low-speed edge than along the high-speed interface.

Probability of Mixed Fluid

From the pure fluid profiles, the probability of mixed fluid profiles $P_m(\eta)$ are generated and plotted in Figure 21. The peak value of P_m is always less than unity even at the midpoint, in agreement with other researchers using chemically reacting and cold chemistry methods (Hall (1991); Clemens and Paul (1995)), although at the higher compressibilities, the chance of finding mixed fluid is better than 95% for a fairly broad region of the mixing layer. With increasing M_c and Re the chance of finding mixed fluid

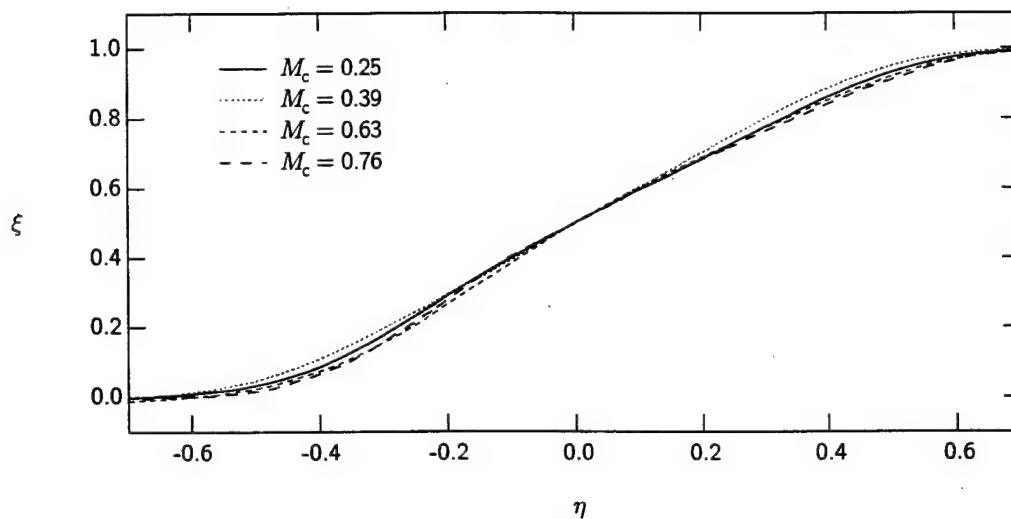


Fig. 17. *Re*-averaged mean composition profiles: fast- and slow-side seeding combined and corrected for air contamination.

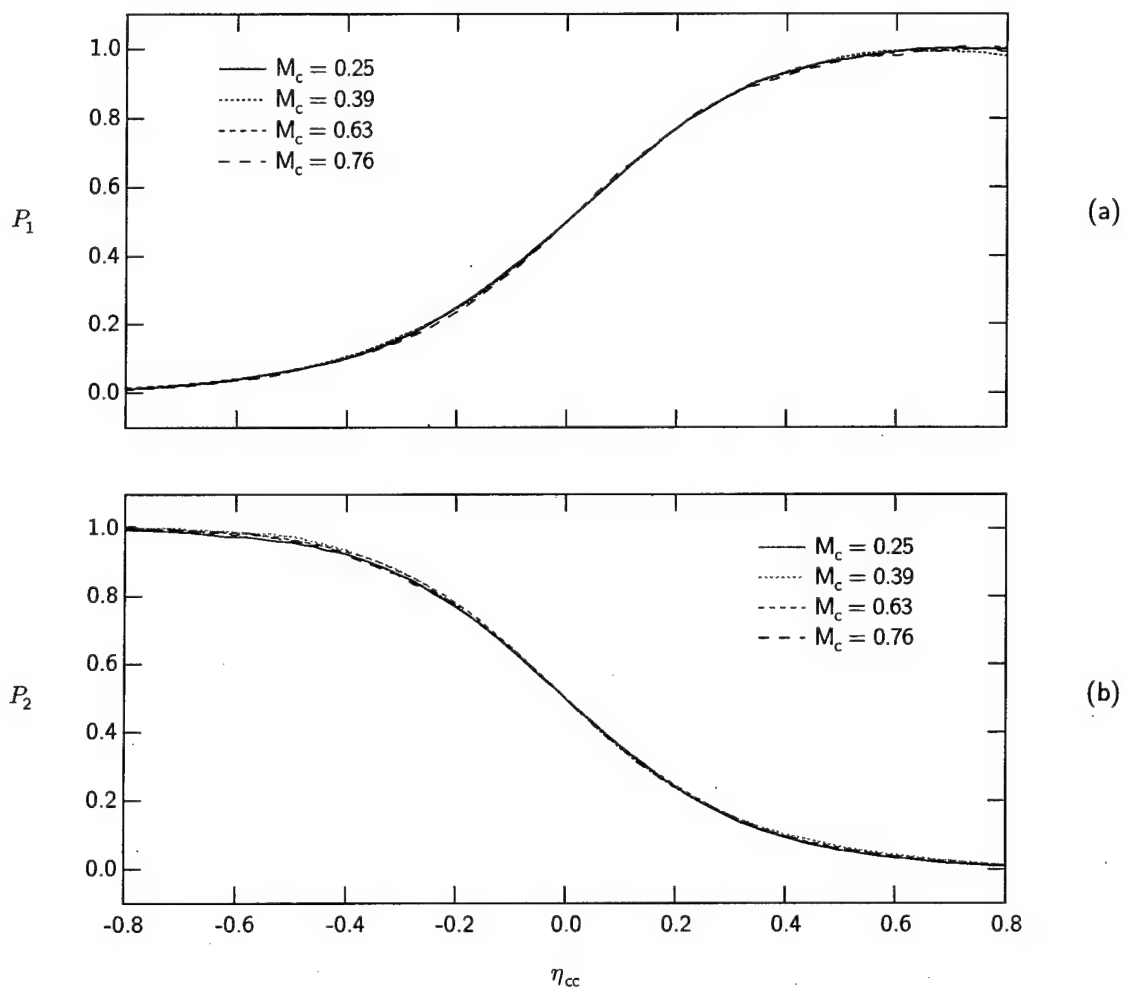


Fig. 18. *Re*-averaged pure fluid profiles obtained with the cold chemistry method. The transverse coordinate η_{cc} is scaled on the cold chemistry data itself.

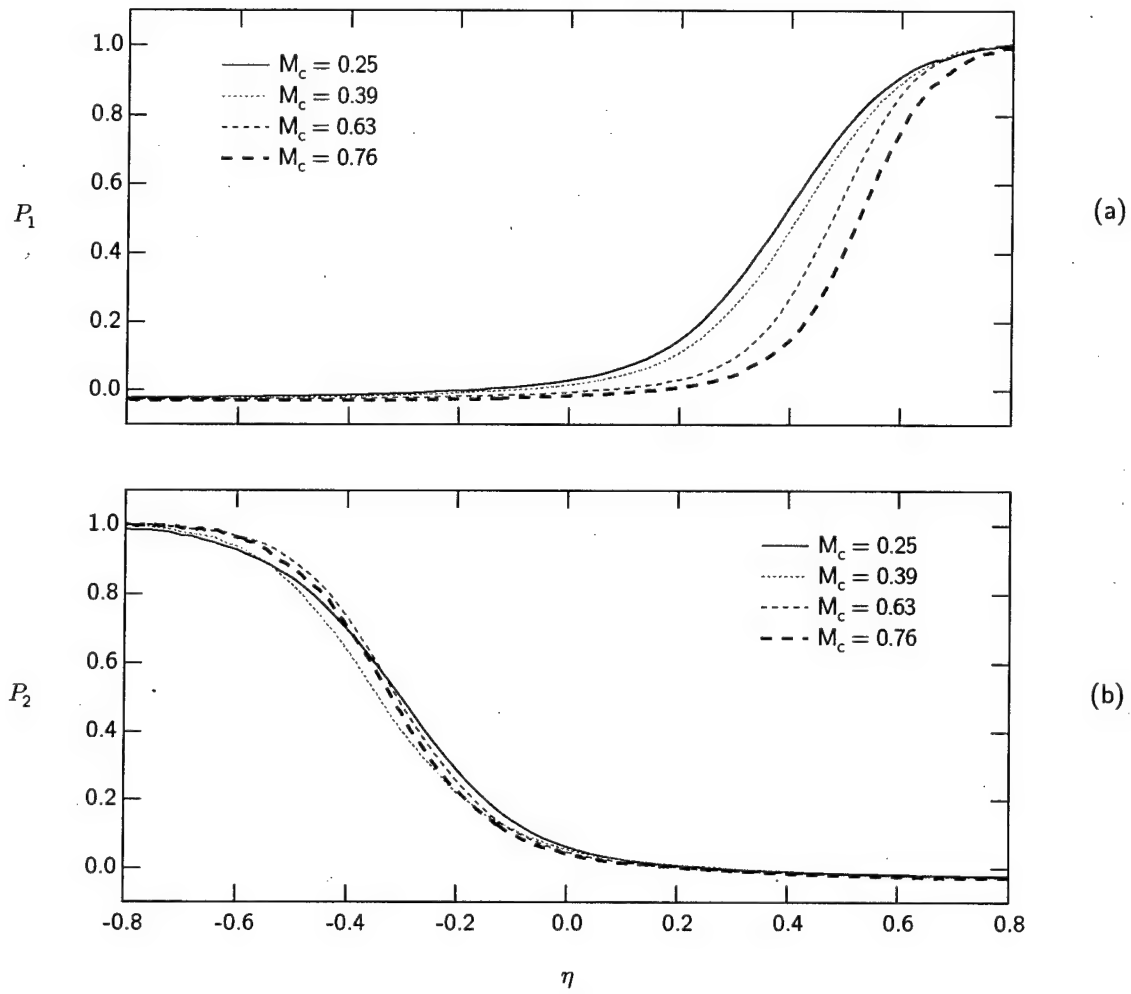


Fig. 19. *Re*-averaged pure fluid profiles obtained with the cold chemistry method. The transverse coordinate η is scaled on the corrected passive scalar mean composition.

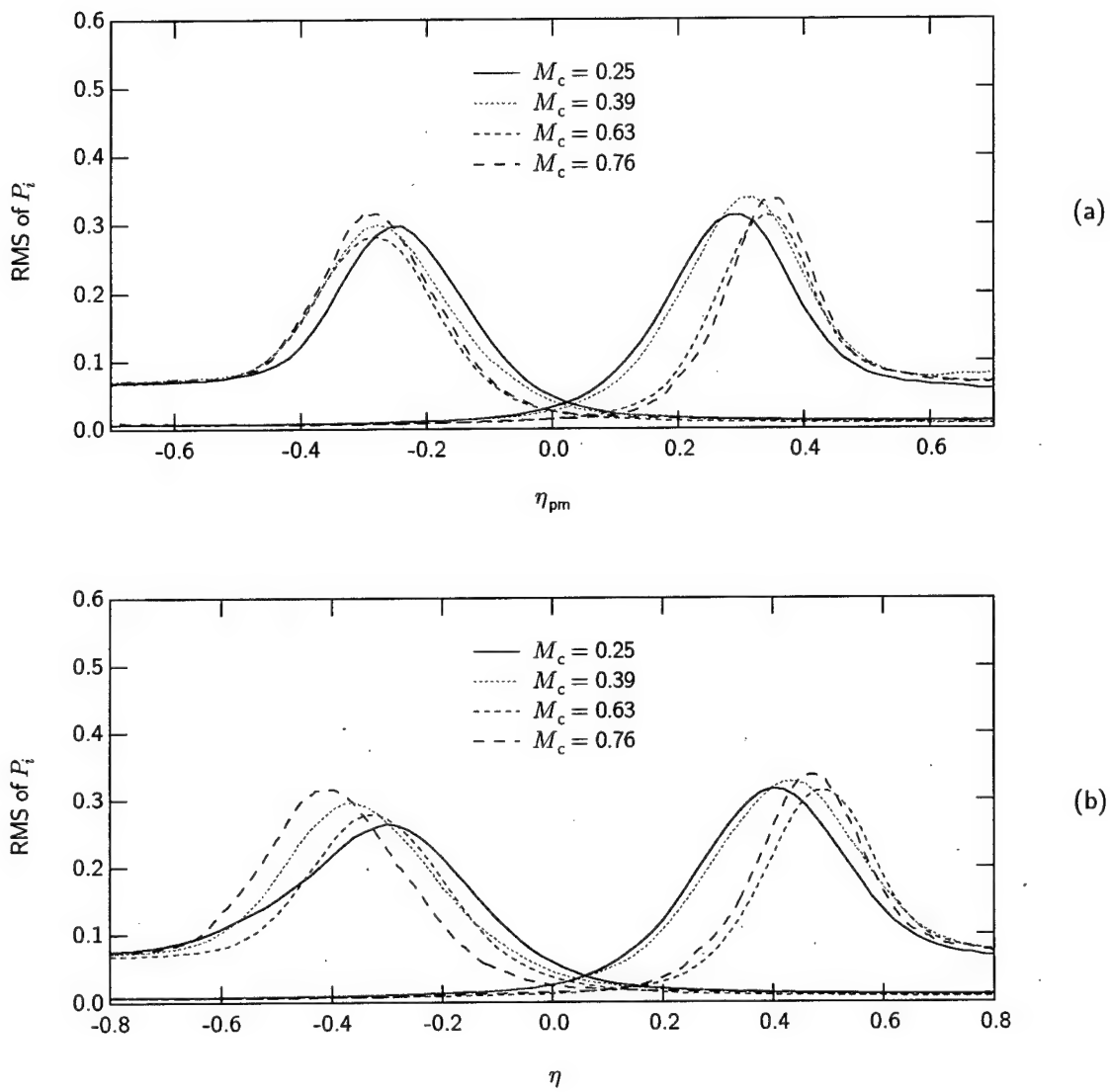


Fig. 20. Re-averaged RMS fluctuations of pure fluid for η scaled on (a) the probability of mixed fluid (cold chemistry) and (b) the corrected mean composition profile (passive scalar).

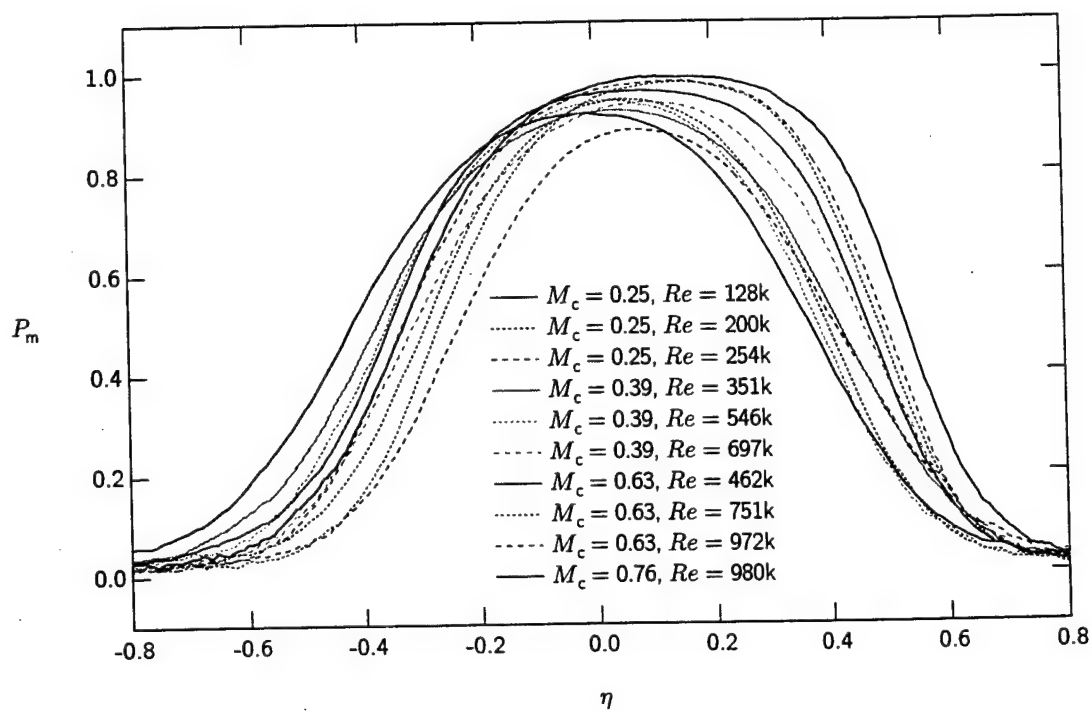
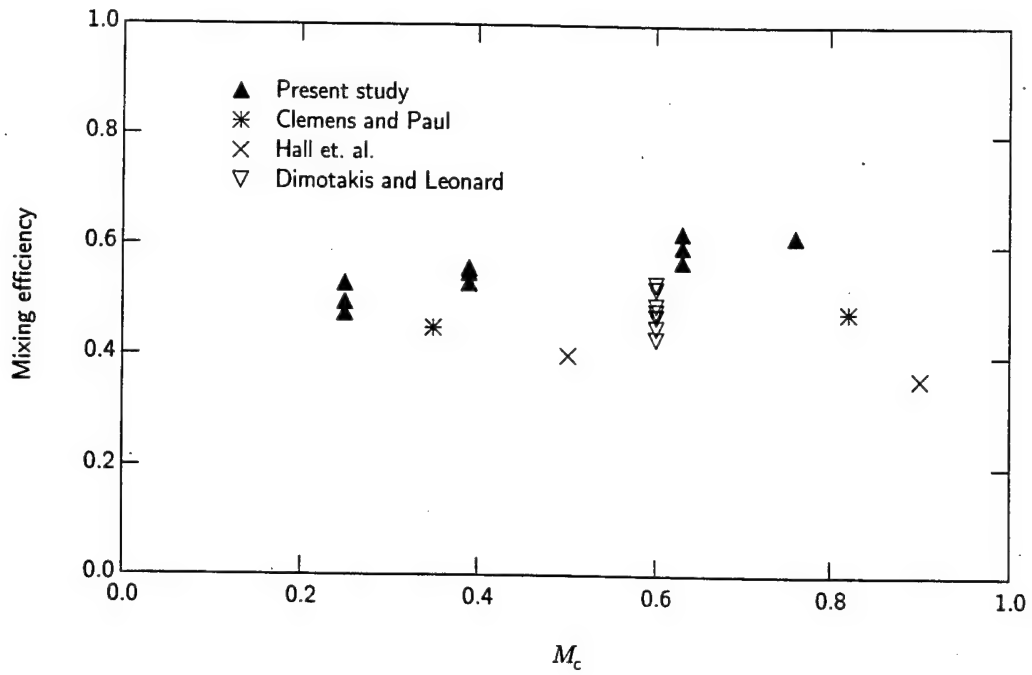
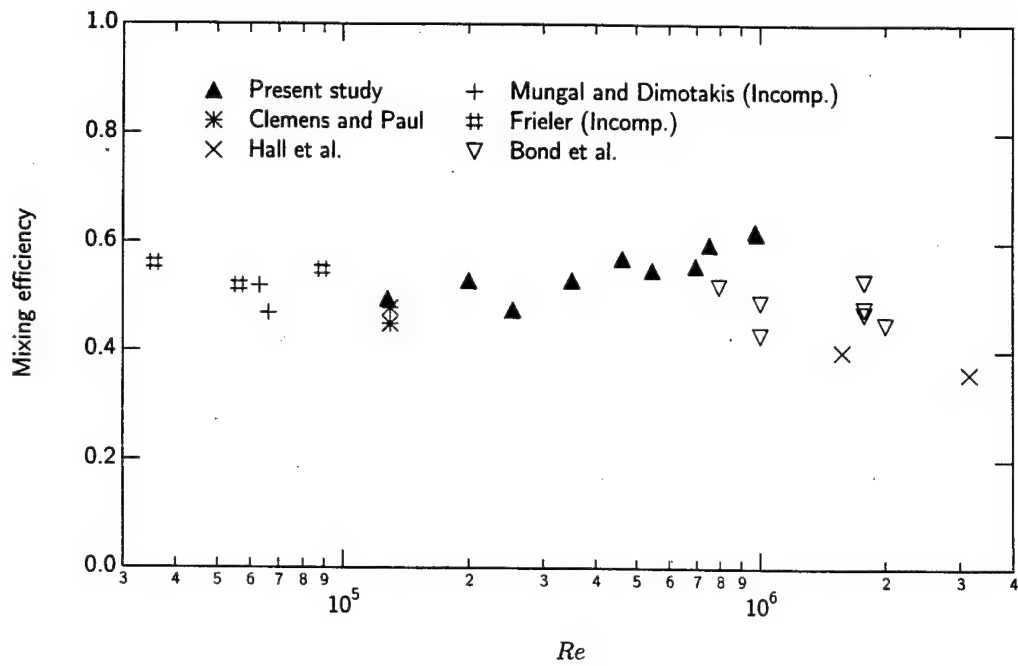


Fig. 21. Probability of mixed fluid profiles from the cold chemistry method, with η scaled on the corrected passive scalar mean composition.



(a)



(b)

Fig. 22. Mixing efficiency as a function of (a) M_c and (b) Re for the present and other resolution-insensitive measurements.

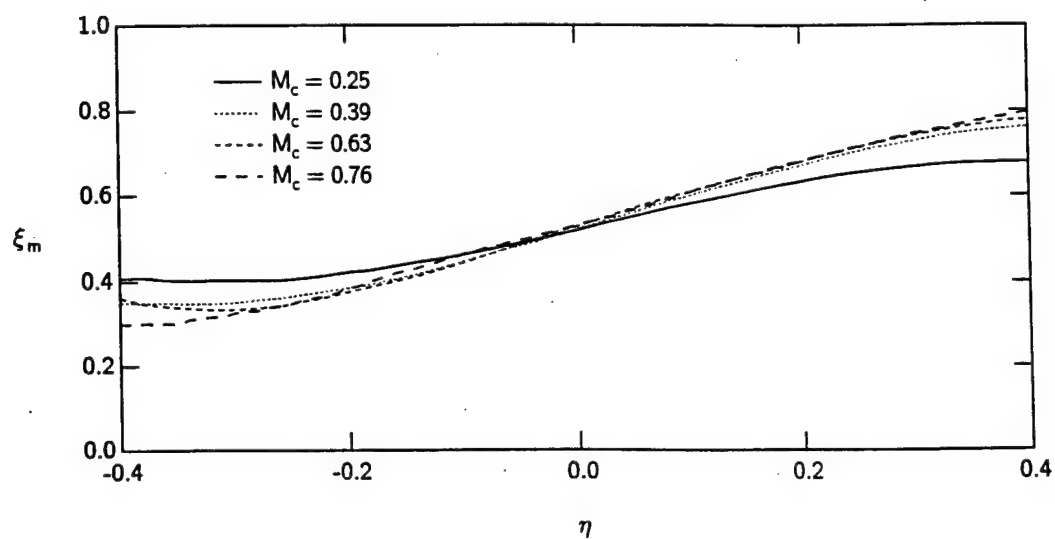


Fig. 23. *Re*-averaged mixed mean composition profiles for combined fast- and slow-side seeding, corrected for air contamination.

becomes biased towards the high-speed interface suggesting that the mixed mean composition near the high-speed edge will increase with compressibility.

The mixing efficiency δ_m/δ denotes the fraction of fluid in the layer which is molecularly mixed and is defined as the integral of the probability of mixed fluid profile $P_m(\eta)$. The mixing efficiencies determined from the 10 cold chemistry flip experiments are plotted versus convective Mach number in Figure 22(a) and Reynolds number in Figure 22(b). As displayed in Figure 22(a), there is an apparent trend of moderately increasing mixing efficiency with increasing compressibility, with $\delta_m/\delta = 0.50, 0.55, 0.60$, and 0.62 at $M_c = 0.25, 0.39, 0.63$, and 0.76 , respectively. Hall (1991), using a chemical reaction method in planar mixing layers, found mixing efficiency to decline by 15% between $M_c = 0.5$ and 0.9 ; however, his technique suffers from relatively poor equivalence ratio ($\phi=1/4$) and potential finite rate chemistry effects due to short fluid mechanical time scales in the compressible mixing layer.

The apparent trend of increased mixing efficiency with compressibility seen in the present experiments, however, may be attributable to Reynolds number effects. As seen in Figure 22(b), the present results show a strong correlation of increased mixing efficiency with Re , approximately 20% per decade. Except for a single point at low compressibility, each of the experiments conducted at a given compressibility shows an increase in δ_m/δ with Re . Additionally, the highest compressibility point has nearly the same Re as one of the $M_c = 0.63$ cases and has a similar mixing efficiency, despite a 21% increase in M_c . The strong correlation between δ_m/δ and Re seems to largely account for the change in efficiency seen with compressibility, and we therefore conclude that mixing efficiency is essentially independent of compressibility.

Mixed Mean Composition

As discussed earlier, the mixed mean composition ξ_m , *i.e.*, the average high-speed mixture fraction of fluid which has been mixed, is calculated by subtracting the component of pure fluid as determined by the cold chemistry measurement from the mean composition determined by the passive scalar technique. Figure 23 displays the results. Increased compressibility appears to shift the mixed mean away from a preferred value and toward a more continuous or freestream-biased profile. This trend is associated with compressibility and not density ratio because the highest and lowest compressibility cases have approximately the same density ratio. Note that most of the change appears to occur along the high-speed interface and that even under compressible conditions little of the mixed fluid, on average, is comprised of more than 80% freestream fluid. Again,

these results should be regarded cautiously since the passive scalar component is subject to air contamination in the more compressible cases. The present results generally support the reacting results of Miller *et al.* (1997) and would explain more intense OH in compressible cases.

5.2.4 Mixing Enhancement

In the mixing enhancement study, sub-boundary layer disturbances were introduced by applying small pieces of Scotch tape having a thickness of 60 microns to the high-speed (supersonic) side of the splitter tip as shown in Figure 24. The geometric parameters varied were 1) shape of the disturbance (from sharp triangles to squares) as determined by ϕ , 2) number N of disturbances, 3) obliquity θ of an array of disturbances, 4) offset L_0 from the splitter tip, and 5) thickness t (height from the splitter tip surface) of the disturbance. The thickness was varied by layering the Scotch tape and ranges from 5 to 50% of the calculated splitter tip boundary layer displacement thickness δ_{99} . Additionally, two-dimensional disturbances with single or double spanwise trips, as shown in Figure 24(d), were tested for smooth and rough surfaces. For each geometry, time resolved end, side, and plan view visualizations of mixed fluid were obtained with the planar laser Mie scattering (PLMS) technique. The product formation method was used whereby alcohol droplets condense in mixed fluid and high scattering signal consequently marks mixed fluid.

5.2.5 Mixing Enhancement Results: Images

Schlieren

For reference, Toepler schlieren side view images are shown in Figure 25 for the $M_c = 0.76$ case with and without a disturbance. The disturbance geometry consists of five discrete equilateral triangles located on the end of the splitter tip, with a thickness one-half of the calculated boundary layer displacement thickness.

For the unperturbed case, Figure 25(a) shows the shock structure and mixing layer for the first 12 cm of the test section. The shock originating upstream of the splitter tip is a result of the (very) slight mismatch between the nozzle wall and upper guidewall, and a second shock is generated from the flow expansion at the end of the splitter. The mixing layer grows approximately linearly from a virtual origin upstream of the splitter tip. In the close-up shown in Figure 25(b), the high-speed boundary layer can just be discerned, especially in the average view.

For the perturbed case, Figure 25(c) shows a dramatic increase in the mixing layer thickness and increased growth rate, with δ about twice that of the unperturbed case. Since Toepler schlieren integrates across the mixing layer, it cannot, however, distinguish between the entire layer thickening or the presence of spanwise convolutions. Most of the increased growth occurs along the low-speed interface and the virtual origin shifts towards the splitter tip. Comparing to Figure 25(a), a new shock is evident that originates upstream of the splitter tip and penetrates the mixing layer after reflection from the upper wall. From the close-up average in Figure 25(d), this shock can be seen to originate from the upstream edge of the disturbance. Although this is the thickest disturbance investigated, Figure 25(d) shows it well within the (thermal) boundary layer.

PLMS

For brevity, planar laser Mie scattering images at the $M_c = 0.63$ flow condition are presented here (see Figure 26) only for the same geometry as the Schlieren images. Flow is left to right with instantaneous and average (a) plan views, (b) end views, and (c) side views. The plan views of Figure 26(a) clearly indicate streamwise structure which is well-localized, as seen in the average. Even with the thin disturbance ($t/\delta_{99} = 5\%$) used in the end view imaging, significant spanwise convolutions can be discerned. The bottom end view image is included as a typical example that suggests the presence of counter-rotating vortex pairs associated with the discrete disturbances. To be objective, there is considerable variation in the end views in all cases, but images suggesting counter-rotating vortices are both more frequent and more consistent for discrete 3D disturbances compared to the unperturbed case. The side views of Figure 26(b) also indicate a thicker mixing layer for this case relative to the unperturbed case.

5.2.6 Mixing Enhancement Results: Statistics

The mixing layer thickness was measured directly from the side and end view PLMS images to examine the effect of different disturbance geometries. The most significant results are described below and further detail can be found in Island (1997).

Shape

The effects of disturbance shape on mixing layer thickness is shown in Figure 27 which plots the normalized thickness as a function of shape parameter ϕ . Both the end view measurements (top) and side view measurements (bottom) suggest that the optimal shape is an equilateral triangle $\phi = 30$ degrees. The most conclusive data comes from the thicker disturbances in the side view measurement where the thickness is 20% greater for

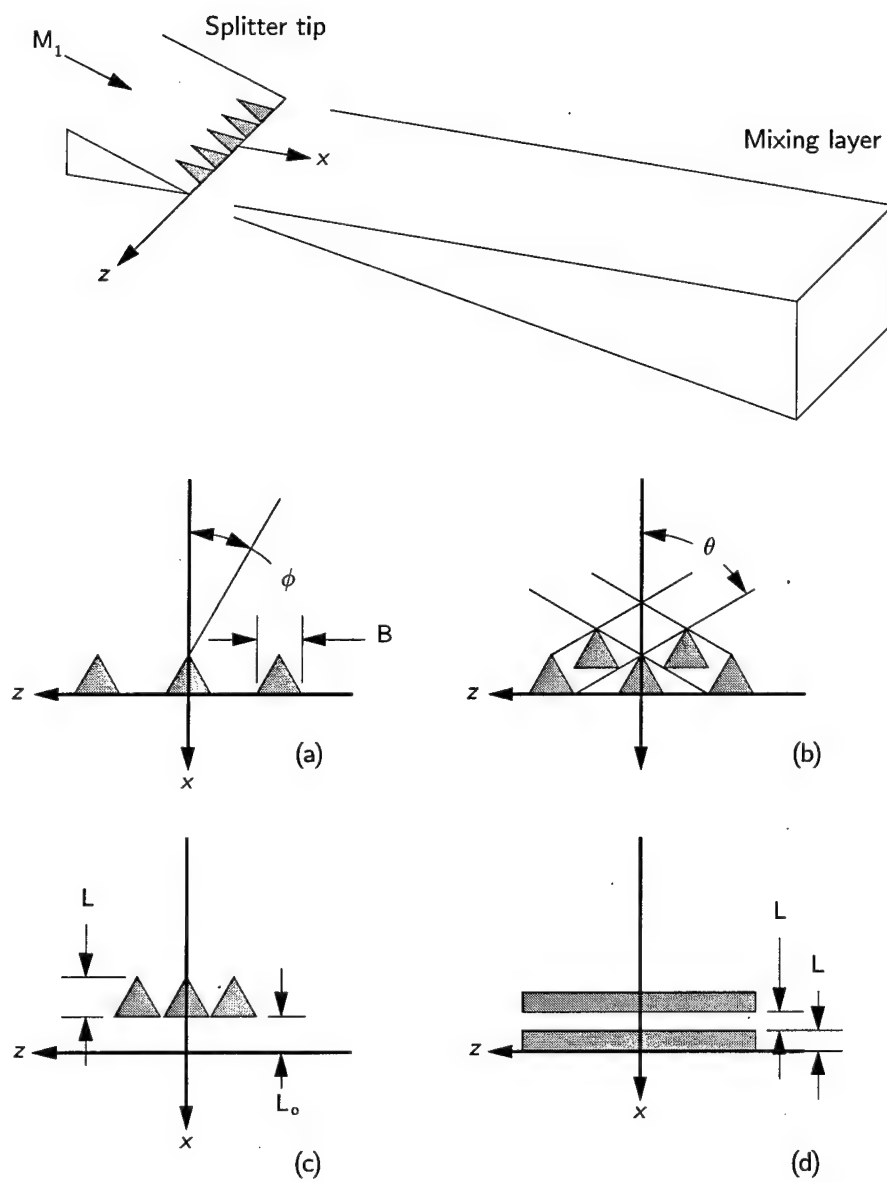


Fig. 24. Defining geometry for the mixing enhancement disturbances.

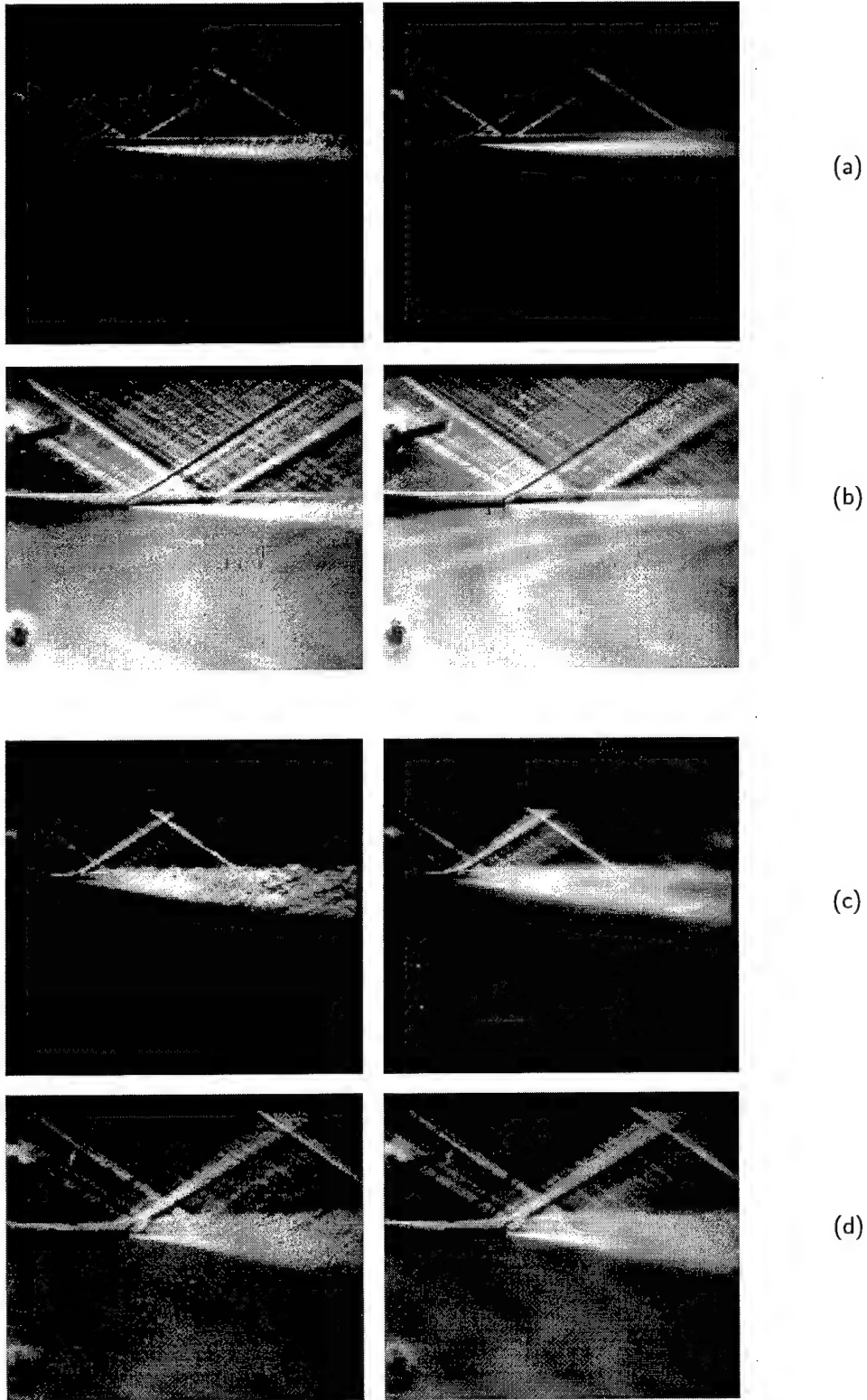


Fig. 25. Schlieren images at $Mc = 0.76$ for (a) unperturbed wide view, (b) unperturbed close-up, (c) perturbed wide view, and (d) perturbed close-up. Shown are (left) instantaneous and (right) averaged images.

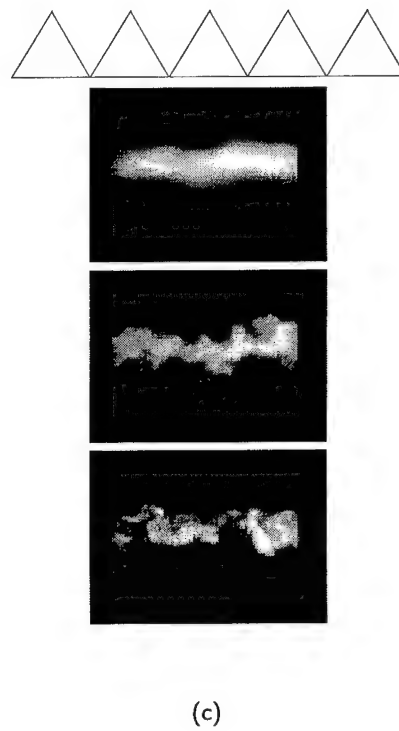
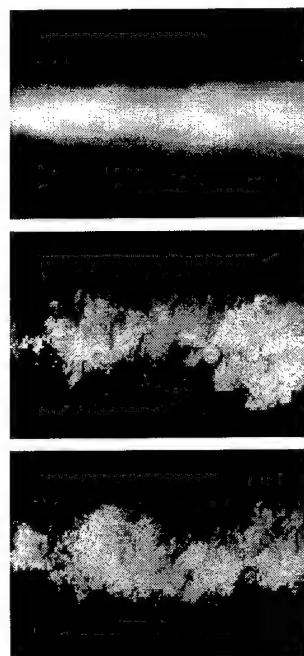
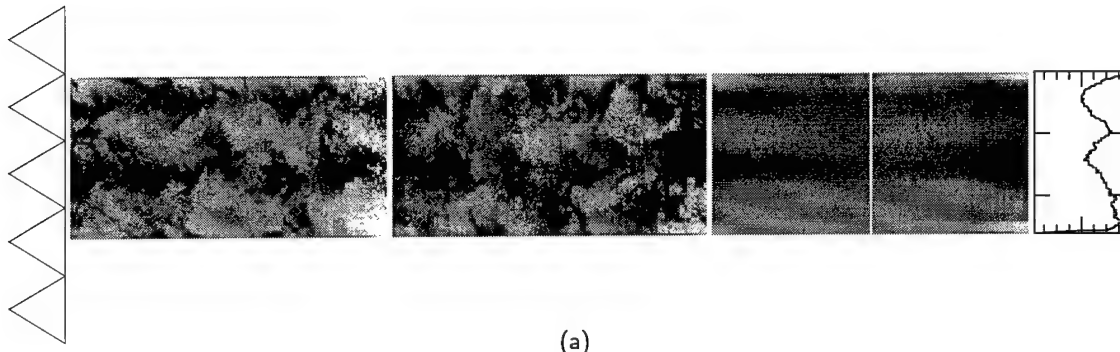


Fig. 26. Typical instantaneous and average PLMS images for (a) plan, (b) side, and (c) end views for the case 3 geometry. The disturbance thickness is $t/\delta_{99} = 25\%$ for the plan and side views and $t/\delta_{99} = 5\%$ for the end views.

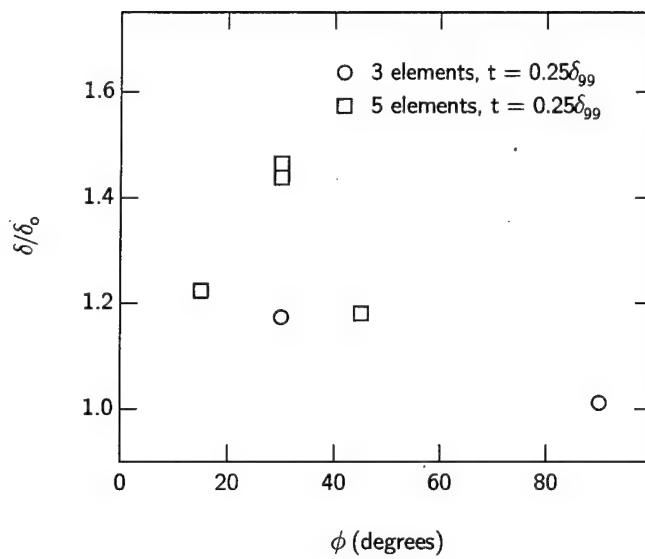
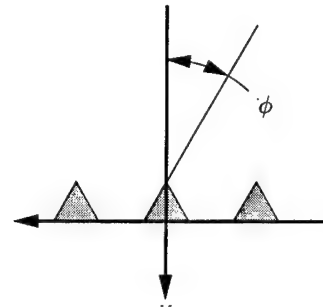
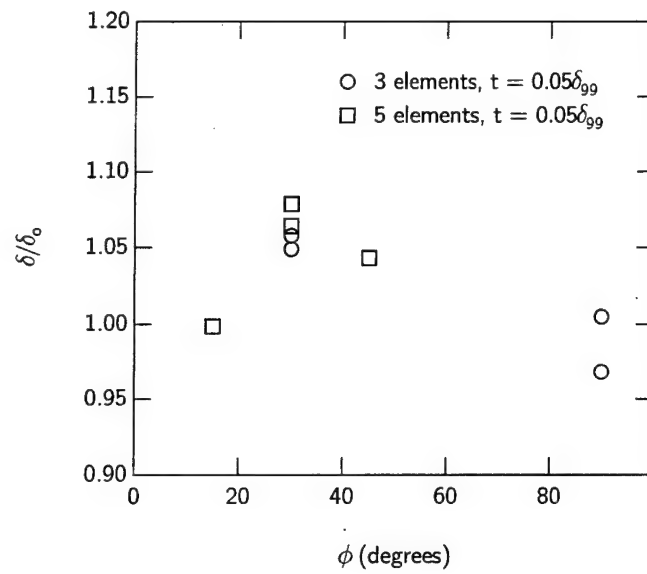


Fig. 27. Normalized mixing layer thickness δ/δ_0 with different shape elements measured from (top) end views and (bottom) side views. As shown, the shape is specified by the angle ϕ relative to the streamwise direction, so that a square is 90° and an equilateral triangle is 30° .

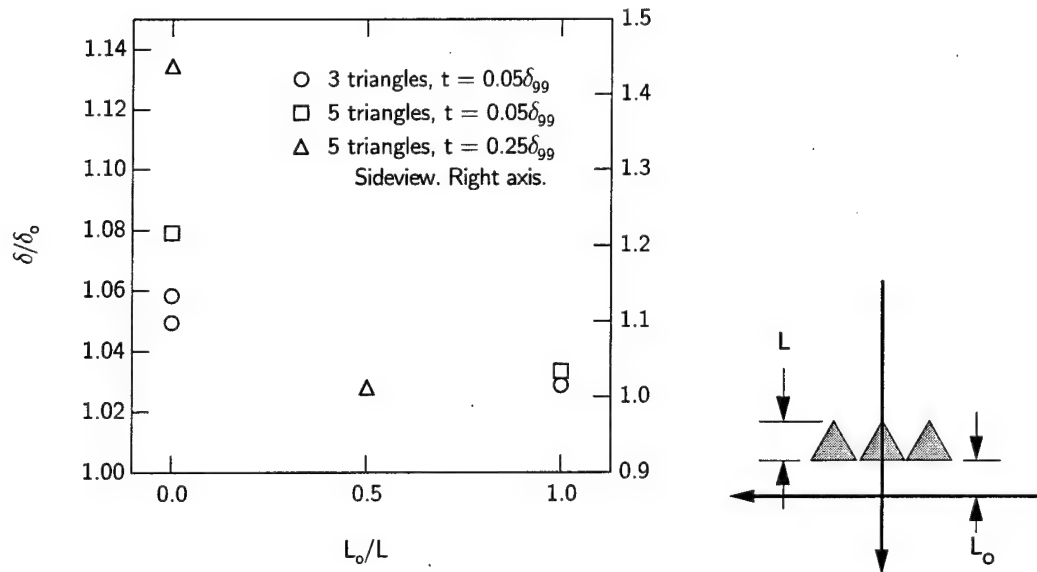


Fig. 28. Normalized mixing layer thickness δ/δ_0 at different offsets L_0/L from the splitter tip, as defined in the right figure. Determined from side and end views.

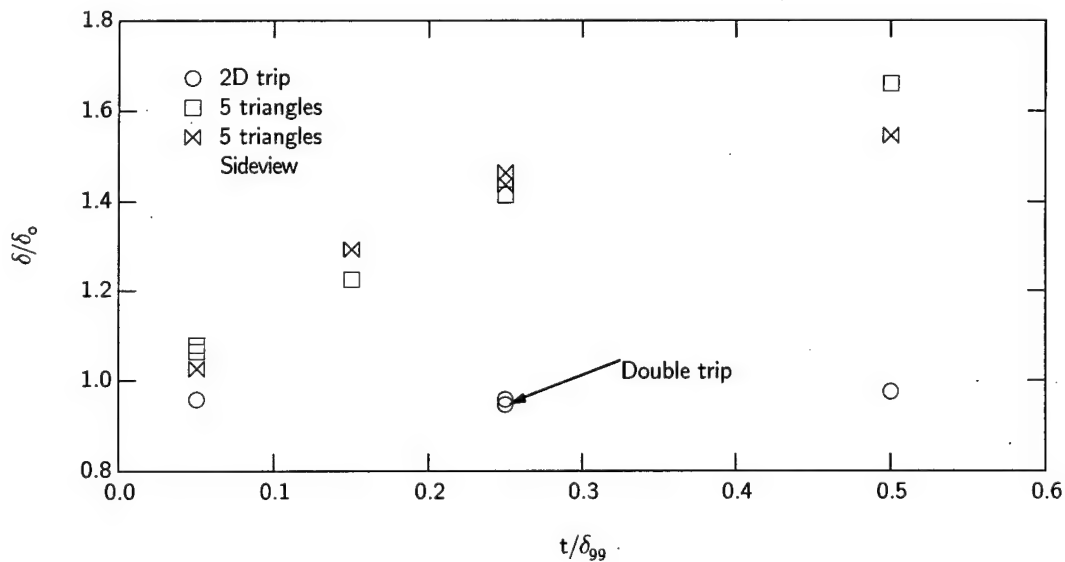


Fig. 29. Normalized mixing layer thickness δ/δ_0 for 2D and 3D triangular perturbations of different thickness. The disturbance thickness δ/δ_{99} is normalized on the high-speed boundary layer displacement thickness. Determined from side and end views.

an equilateral triangle compared to the more and the less acute triangles tested. Note that the flow area blockage is the same for all the shapes tested so we expect roughly the same pressure losses associated with each shape. Square shapes ($\phi = 90$ degrees) were found to be the least effective at enhancing thickness even though the images do show a moderate increase in streamwise structure.

Offset

The impact of offsetting the disturbances from the splitter tip is shown in Figure 28. As also suggested by the images, the largest improvement in δ occurs for disturbances placed directly at the splitter tip. Again, the most dramatic evidence comes from the thicker disturbances measured in side view which show a 45% improvement in δ for disturbances with zero offset as opposed to almost no improvement for an offset of $L_o/L = 1/2$.

Disturbance Thickness and 2D vs. 3D Effects

Figure 29 plots the improvement in layer thickness versus the disturbance thickness for discrete triangular and 2D disturbances. The triangular disturbances dramatically increase the layer thickness with a 30 and 60% thickening for a disturbance thickness of 15 and 50% of the boundary layer, respectively. Equally notable is the negative result for the 2D and double 2D spanwise disturbance which actually slightly decrease the layer thickness, despite having equivalent flow blockage as the triangles. Smooth (Scotch tape) and rough (400 and 120 grit sandpaper) 2D disturbances show similar results.

5.2.7 Mixing Enhancement Results: Quantitative Cold Chemistry Measurements

Cold chemistry measurements were made for the $M_c = 0.63$ flowfield for the most promising enhancement geometry (five equilateral triangles at the splitter tip) having thickness $t/\delta_{99} = 25\%$. The principal findings are: 1) the enhanced case shows a 48% increase in mixing layer thickness compared to the cold chemistry thickness of the unperturbed case at this compressibility and Reynolds number; 2) the probability of pure fluid curves are quite similar between the perturbed and unperturbed cases. The shape of these curves now appears quite robust with near perfect collapse for a ten-fold increase in Re , significant changes in M_c , and unperturbed and moderately perturbed mixing layers; 3) the pure fluid probabilities show greater RMS fluctuation along both interfaces for the enhanced case; 4) for the perturbed case, the probability of finding mixed fluid is essentially unity in the middle 10% of the mixing layer, compared to about a 95%

probability in the unperturbed $M_c = 0.65$ case. Even more than the unperturbed compressible cases, P_m is biased towards the high-speed side. In contrast, along the low-speed edge there is slightly less chance of finding mixed fluid in the enhanced layer; 5) the measured mixing efficiency is $\delta_m/\delta = 0.64$ compared to 0.60 for the unperturbed layer at the same M_c and Re , a 7% increase which is within the uncertainty of the cold chemistry measurements. The enhanced case has, therefore, approximately 57% more mixed fluid, mostly because of the thicker layer.

The quantitative mixing enhancement results are particularly significant because they show that a qualitatively thicker layer can have a correspondingly greater amount of molecularly-mixed fluid. That is, the mixing efficiency of the layer does not decrease as a result of the thickness enhancement and greater bulk entrainment thereby implies greater entrainment into the mixed state, which is the relevant issue for most applications. This result is not necessarily true and does not, of course, universally apply to other enhancement strategies which might thicken the mixing layer by increasing the amount of pure (unmixed) fluid in the layer. However, the constancy of mixing efficiency in this case bodes well for the applicability of the large body of qualitative mixing enhancement results in the literature.

6.0 REFERENCES

- Clemens, N.T. and P.H. Hall (1995). Scalar measurements in compressible axisymmetric mixing layers. *Physics of Fluids A* **5**: 1071-1081.
- Frieler, C.E. (1992). Mixing and reaction in the subsonic 2-D turbulent free shear layer. Ph.D. thesis, California Institute of Technology.
- Hall, J.L. (1991). An experimental investigation of structure, mixing and combustion in compressible turbulent shear layers. Ph.D. thesis, California Institute of Technology
- Houwing, A.F.P., J.L. Palmer, M.C. Thurber, S.D. Wehe, R.K. Hanson, and R. R. Boyce (1996). Comparison of planar fluorescence measurements and computational modeling of shock-layer flow, *AIAA J.* **34**(3): 470-477.
- Island, T.C. (1997). Quantitative scalar measurements and mixing enhancement in compressible shear layers. Ph.D. thesis, Stanford University.
- McMillin, B. K., M. P. Lee, J. L. Palmer, P. H. Paul, and R. K. Hanson (1989). "Planar laser-induced fluorescence imaging of shock-heated flows in vibrational nonequilibrium," B. Khalighi, M. J. Braun and C. J. Freitas, Eds., *Flow Visualization - 1989, FED*, Vol. 85 (The American Society of Mechanical Engineers, New York, NY), pp. 55-62.

McMillin, B. K., M. P. Lee, P. H. Paul, and R. K. Hanson (1990). "Planar laser-induced fluorescence imaging of shock-induced ignition," *Twenty-Third Symposium (International) on Combustion* (The Combustion Institute, Pittsburgh, PA), pp. 1909–1914.

McMillin, B. K., J. L. Palmer, and R. K. Hanson (1991). "Two-dimensional temperature measurements of nonequilibrium supersonic flows using planar laser-induced fluorescence of nitric oxide," AIAA paper 91-1670, AIAA 22nd Fluid Dynamics, Plasma Dynamics and Lasers Conference, Honolulu, HA, Jun. 24–26, 1991.

McMillin, B.K., J.M. Seitzman, and R.K. Hanson (1994). Comparison of NO and OH planar laser-induced fluorescence temperature measurements in SCRAMJET model flowfields, *AIAA J.* **32**(10): 1945–1952.

Miller, M.F., Bowman, C.T. and Mungal, M.G. (1997). An experimental investigation of the effects of compressibility on a turbulent reacting mixing layer. Submitted to *J. Fluid Mech.*

Palmer, J. L., and R. K. Hanson (1993a). "Planar laser-induced fluorescence imaging in free jet flows with vibrational nonequilibrium," AIAA paper 93-0046, AIAA 31st Aerospace Sciences Meeting and Exhibit, Reno, NV, Jan. 11–14, 1993.

Palmer, J. L., and R. K. Hanson (1993b). "Single-shot velocimetry using planar laser-induced fluorescence imaging of nitric oxide," AIAA paper 93-2020, AIAA/SAE/ASME/ASEE 29th Joint Propulsion Conference and Exhibit, Monterey, CA, Jun. 28–30, 1993.

Palmer, J.L., and R.K. Hanson (1995). "Shock tunnel flow visualization using planar laser-induced fluorescence imaging of NO and OH," *Shock Waves* **4**(6): 313–323.

Palmer, J.L., and R.K. Hanson (1996). "Temperature imaging in a supersonic free jet of combustion gases using two-line OH fluorescence," *Appl. Opt.* **35**(3): 485–499.

Palmer, J.L., B.K. McMillin, and R.K. Hanson (1996). "Multi-line fluorescence imaging of the rotational temperature field in a shock-tunnel free jet," *Appl. Phys. B*, **63**(2): 167–178.

Paul, P.H. and N.T. Clemens (1993). Sub-resolution flowfield measurements of unmixedness using electronic quenching of $\text{NO } A^2\Sigma^+$. *Optics Letters* **18**: 161.

Planché, O.H. and Reynolds, W.C. (1992a). A numerical investigation of the compressible reacting mixing layer. Report TF-56, Thermosciences Division, Department of Mech. Eng., Stanford University.

Planché, O.H. and Reynolds, W.C. (1992b) Heat release effects on mixing in supersonic reacting free shear-layers. *AIAA Paper* 92-0092.

Seitzman, J. M., and R. K. Hanson (1993). "Two-line planar fluorescence for temporally resolved temperature imaging in a reacting supersonic flow over a body," *Appl. Phys. B* **57**(6): 385–391.

Seitzman, J.M., R.K. Hanson, P.A. DeBarber, and C.F. Hess (1994). Application of quantitative two-line OH planar laser-induced fluorescence for temporally resolved planar thermometry in reacting flows, *Appl. Opt.* **33**(18): 4000–4012.

6.1. Publications

Clemens, N.T. and M.G. Mungal (1995), Large structure and entrainment in the supersonic mixing layer, *J. Fluid Mech.*, **284**: 171-216.

Day, M.J., N.N. Mansour, W.C. Reynolds (1997b), "The structure of the compressible reacting mixing layer: Insights from linear stability analysis," Submitted to *Physics of Fluids*.

Day, M.J., N.N. Mansour, W.C. Reynolds (1997c), On parametrizing the growth rate influence of the velocity ratio in compressible reacting mixing layers, Submitted to *Physics of Fluids*.

Houwing, A.F.P., J.L. Palmer, M.C. Thurber, S.D. Wehe, R.K. Hanson, and R. R. Boyce (1996). Comparison of planar fluorescence measurements and computational modeling of shock-layer flow, *AIAA J.* **34**(3): 470-477.

Island, T.C., B.J. Patrie, M.G. Mungal and R.K. Hanson (1996), Instantaneous three-dimensional flow visualization of a supersonic mixing layer, *Expts. Fluids* **20**: 249-256.

McMillin, B.K., J.M. Seitzman, and R.K. Hanson (1994). Comparison of NO and OH planar laser-induced fluorescence temperature measurements in SCRAMJET model flowfields, *AIAA J.* **32**(10): 1945-1952.

Miller, M.F., C T. Bowman and M.G. Mungal (1997), An experimental investigation of the effects of compressibility on a turbulent reacting mixing layer. Submitted to *J. Fluid Mech.*

Palmer, J.L., and R.K. Hanson (1995). "Shock tunnel flow visualization using planar laser-induced fluorescence imaging of NO and OH," *Shock Waves* **4**(6): 313-323.

Palmer, J.L., and R.K. Hanson (1996). "Temperature imaging in a supersonic free jet of combustion gases using two-line OH fluorescence," *Appl. Opt.* **35**(3): 485-499.

Palmer, J.L., B.K. McMillin, and R.K. Hanson (1996). "Multi-line fluorescence imaging of the rotational temperature field in a shock-tunnel free jet," *Appl. Phys. B*, **63**(2): 167-178.

Seitzman, J.M., R.K. Hanson, P.A. DeBarber, and C.F. Hess (1994). Application of quantitative two-line OH planar laser-induced fluorescence for temporally resolved planar thermometry in reacting flows, *Appl. Opt.* **33**(18): 4000-4012.

6.2. Presentations

Day, M.J., N.N. Mansour and W.C. Reynolds (1995), "Linear Stability Regime Analysis of the Compressible Reacting Mixing Layer," presented at the 48th APS/DFD Meeting, Irvine, CA.

Day, M.J., N.N. Mansour and W.C. Reynolds (1996), "Linear Stability and Structure of the Compressible Reacting Mixing Layer," presented at the 49th APS/DFD Meeting, Syracuse, NY.

Day, M.J., N.N. Mansour, W.C. Reynolds (1997a), "Linear Stability and Structure of the Compressible Reacting Mixing Layer," paper AIAA 97-0761, AIAA 35th Aerospace Sciences Meeting, Reno, NV.

Island, T. C. Island, W.D. Urban and M.G. Mungal (1997), "Small Perturbation Mixing Enhancement in Compressible Shear layers", AIAA-97-0395, 35th AIAA Aerospace Sciences Meeting, Reno, NV.

Island, T.C., W.D. Urban and M.G. Mungal (1996), "Quantitative Scalar Measurements in Compressible Mixing Layers", AIAA-96-0685, 34th AIAA Aerospace Sciences Meeting, Reno, NV.

Island, T.C., W.D. Urban and M.G. Mungal, "Quantitative Scalar Measurements in Compressible Mixing Layers", Bull. Amer. Phys. Soc., 40 (12), 1975, Nov. 1995.

Miller, M.F., J.M. Seitzman, C.T. Bowman and M.G. Mungal, "Evolution of Large-Scale Structures in Reacting Mixing Layers", Bull. Amer. Phys. Soc., 39 (9), 1895, Nov. 1994.

Urban, W.D. and M.G. Mungal (1997), "Planar Velocity Measurements in Compressible Mixing Layers", AIAA-97-0757, 35th AIAA Aerospace Sciences Meeting, Reno, NV.

7.0 PERSONNEL

Craig T. Bowman	Professor, Mechanical Engineering
Ronald K. Hanson	Professor, Mechanical Engineering
Mark Godfrey Mungal	Associate Professor, Mechanical Engineering
William C. Reynolds	Professor, Mechanical Engineering
Mark Day	Graduate Research Assistant, Mechanical Engineering
Tobin Island	Graduate Research Assistant, Mechanical Engineering
Michael F. Miller	Graduate Research Assistant, Mechanical Engineering
Jennifer Palmer	Graduate Research Assistant, Mechanical Engineering
William D. Urban	Graduate Research Assistant, Mechanical Engineering

8.0 PH.D. DEGREES AWARDED

Michael F. Miller, 1994, "An Experimental Investigation of the Effect of Compressibility on a Turbulent Reacting Mixing Layer"

Tobin C. Island, 1997, "Quantitative Scalar Measurements and Mixing Enhancement in Compressible Shear Layers"